

# GeN-ROM—An OpenFOAM<sup>®</sup>-based multiphysics reduced-order modeling framework for the analysis of Molten Salt Reactors

Péter German<sup>a,\*</sup>, Mauricio Tano<sup>a</sup>, Carlo Fiorina<sup>b</sup>, Jean C. Ragusa<sup>a</sup>

<sup>a</sup> Department of Nuclear Engineering, Texas A&M University, 423 Spence St, College Station, TX 77843, USA

<sup>b</sup> Laboratory of Reactor Physics and Systems Behaviour, École Polytechnique Fédérale de Lausanne, PH D3 465, Station 3, CH-1015, Lausanne, Switzerland

## ARTICLE INFO

### Keywords:

Model Order Reduction  
Reduced-order model  
Proper Orthogonal Decomposition  
Multiphysics  
Molten Salt Fast Reactor  
OpenFOAM

## ABSTRACT

This work presents a projection-based multiphysics Model Order Reduction (MOR) framework for the analysis of nuclear systems and its application to parametric simulations of Molten Salt Reactors (MSR). The framework, named GeN-ROM, is developed using OpenFOAM<sup>®</sup> and employs a Proper Orthogonal Decomposition aided Reduced-Basis technique (POD-RB). It can be used to reduce steady-state and transient multiphysics problems involving parametric fluid dynamics, heat exchange, and neutronics phenomena. For the treatment of structural elements in the hydraulic systems, a porous medium approach has been adopted. The reduction process is data-driven and snapshot information is extracted via POD to learn the solution manifold and to build global spatial basis functions. At the data collection phase, GeN-ROM makes use of the solvers available in GeN-Foam, a similarly OpenFOAM<sup>®</sup>-based multiphysics framework developed for the analysis of nuclear reactors. The global bases are used both to approximate the solution fields and to project the full-order equations onto lower-dimensional subspaces, thus considerably reducing the number of unknowns in a numerical system. This reduction leads to significant computational speedups, which is ideal for multi-query applications such as uncertainty quantification or design optimization. The developed tool has been tested using a 2D multiphysics model of the Molten Salt Fast Reactor (MSFR) with steady-state and transient scenarios, with speedups on the order of  $10 - 10^5$ .

## 1. Introduction

Numerical simulations are essential for the design and analysis of nuclear energy systems. The multiphysics treatment of these simulations has become more common, due to advances in computer hardware and simulation software, thus accounting for the multi-way interactions between different physical phenomena. However, full-scale multiphysics simulations are still computationally expensive since they involve not only the numerical solution of large systems for each single physics component but also multiphysics coupling iterations across them. Multi-query applications, such as uncertainty quantification or design optimization, require the repeated simulations of a given system with a large number of model parameter realizations and are frequently used throughout the design and licensing of nuclear reactors. However, due to the computational cost of high-fidelity multiphysics simulations (e.g., thermal hydraulics Wang et al., 2021), multi-query applications can often be prohibitively expensive. Model Order Reduction (MOR) has the potential of alleviating this computational burden by yielding fast-running Reduced-Order Models (ROMs) that can be used as

emulators of higher-fidelity models, and thus accelerating multi-query applications considerably.

This paper introduces GeN-ROM,<sup>1</sup> an OpenFOAM<sup>®</sup>-based (Jasak, 1996; Jasak et al., 2007) multiphysics MOR tool and demonstrates its applicability to multiphysics problems in liquid-fuel Molten Salt Reactors (MSRs). Liquid-fuel MSRs possess unique design and safety features that introduce novel computational challenges since they require the coupled simulation of fluid dynamics, heat transfer, and neutronics phenomena, including precursor drift. Therefore, they offer an apt platform to develop and illustrate the capabilities of a multiphysics ROM framework. Our framework is capable of generating intrusive Proper Orthogonal Decomposition aided Reduced-Basis (POD-RB) ROMs (Pearson, 1901; Pinnau, 2008; Sirovich, 1987; Hesthaven et al., 2016) for partially and fully coupled steady-state and transient problems in MSRs. The choice of POD-RB can be justified by the fact that it has proven to produce efficient emulators for nonlinear and parametric problems, which is the case for many nuclear systems (Ragusa and Mahadevan, 2009). GeN-ROM primarily utilizes the solvers

\* Corresponding author.

E-mail addresses: [peter.german@tamu.edu](mailto:peter.german@tamu.edu) (P. German), [mtano@tamu.edu](mailto:mtano@tamu.edu) (M. Tano), [carlo.fiorina@epfl.ch](mailto:carlo.fiorina@epfl.ch) (C. Fiorina), [jean.ragusa@tamu.edu](mailto:jean.ragusa@tamu.edu) (J.C. Ragusa).

<sup>1</sup> GeN-ROM repository: <https://gitlab.com/peter.german/gen-rom>, Accessed: 09/01/2021.

present in GeN-Foam (General Nuclear Foam) (Fiorina et al., 2015; Radman et al., 2021), an OpenFOAM<sup>®</sup>-based multiphysics framework, for training the ROMs. However, for certain standalone simulations of thermal hydraulics problems, it can also be used with the default OpenFOAM<sup>®</sup> solvers.

In this work, we employ (intrusive) projection-based MOR and thus access and manipulate the discretized operators of the higher-fidelity numerical models. Higher-fidelity numerical models are often referred to as Full-Order Models (FOMs). Non-intrusive MOR also exist but they are not the topic of the present work. For standalone fluid dynamics problems in nuclear engineering, methods rooted in intrusive POD-RB have been utilized for the Lead-Cooled Fast Reactor (LFR) (Lorenzi et al., 2017) and for the Molten Salt Fast Reactor (MSFR) (German et al., 2020, 2021). Intrusive ROMs for standalone radiation transport and diffusion problems have been extensively investigated in Tano et al. (2021b), Sun et al. (2020), Buchan et al. (2015), Behne et al. (2016) and German and Ragusa (2019), Buchan et al. (2013), Sartori et al. (2016, 2014), Lorenzi (2018), Prince and Ragusa (2019), respectively. The development of intrusive ROMs for multiphysics problems is, however, less common. The dominant approach at the moment is the utilization of non-intrusive methods like Polynomial Chaos Expansion (PCE) (Santanoceto et al., 2021) or Sparse Grid Interpolation (Alsayyari et al., 2020). However, non-intrusive techniques may require an immense amount of training data if the function describing the quantities of interest (QoI) is not extremely smooth. For this reason, these works often use fixed velocity fields to reduce the training costs. Aiming at further reduction in training data needs, intrusive approaches have been emerging for multiphysics computations. For example, intrusive POD-RB-ROMs for coupled fluid dynamics and energy equations have been introduced in Vergari et al. (2020), Star et al. (2019) and Tano et al. (2021a) for laminar and Georgaka et al. (2020) for turbulent flows using a RANS approach. The coupling between intrusive ROMs for the energy and neutronics equations have been investigated in Sartori et al. (2016) with a linearized temperature dependence for the cross sections and in German et al. (2019) for arbitrary temperature functions. There are only a few occurrences of intrusive POD-RB-ROMs with complex couplings between equations describing the neutronics, heat transfer and fluid dynamics behavior of nuclear systems. One of the first attempts for such problems was the hybrid ROM developed for a simplified MSR geometry in Panico (2019) with clean laminar fluid flows and a Radial Basis Function (RBF) interpolation for the determination of the group constants. This approach essentially decoupled the energy and neutronics equations at reduced-order level. Improving on this, a linearized cross section dependence was used in Vergari et al. (2021) to develop a ROM for the same simplified MSR geometry with a laminar fluid flow with an artificially large viscosity. Building on these previous efforts, the current work provides a tool which can be used to solve fully coupled multiphysics problems with arbitrary temperature dependence for the neutronics cross sections. Furthermore, GeN-ROM includes tools for time-dependent and eigenvalue neutronics simulations and additional ROMs for adjoint problems for the determination of properties like the effective delayed neutron fraction. Additionally, the method and framework presented here is based on the porous medium formulation of the fluid dynamic equations meaning that it allows the simulation of nuclear systems with structural elements, instead of clean fluid alone. In brief, the presented model provides all the functionalities expected to perform state-of-the-art simulations of nuclear systems at a reduced-order level. The primary goal of this paper is to focus on the multiphysics couplings within the developed GeN-ROM tool while providing key references and appendices for numerical details.

The rest of the paper is organized as follows. Section 2 introduces the implemented intrusive POD-RB method using a general scalar transport equation. Following this, Section 3 discusses the governing equations used to model the behavior of an MSR. Section 4 shows the generation of the specific multiphysics ROMs, while Section 5 describes how the ROMs are evaluated in this work. Lastly, Section 6 shows steady-state and transient numerical experiments using a 2D model of the Molten Salt Fast Reactor (MSFR) (Rouch et al., 2014).

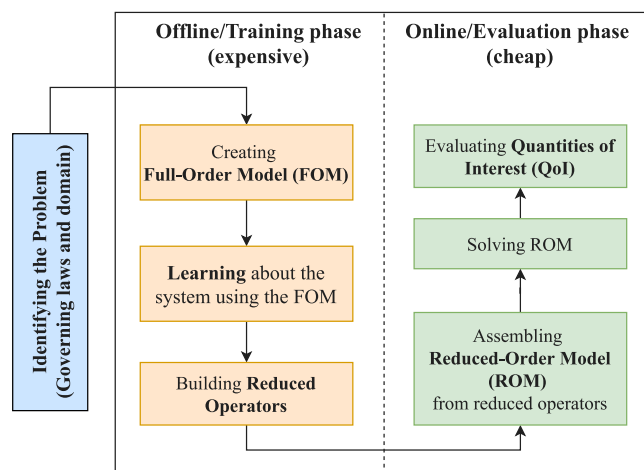


Fig. 1. Flow chart of the POD-RB procedure in this work. Source: Modified based on German et al. (2020), reprinted from German et al. (2021).

## 2. Intrusive Proper Orthogonal Decomposition aided Reduced-Basis Method (POD-RB)

The MOR procedure presented in this work is based on an intrusive Proper Orthogonal Decomposition aided Reduced Basis method (POD-RB). Fig. 1 introduces the necessary steps of the process which starts by the identification of the problem, followed by steps that can be grouped into two phases: an *offline* or *training* phase and an *online* or *evaluation* phase.

In this section, we assume that the problem is a general, nonlinear partial differential equation (PDE) in the following form:

$$\frac{d\theta(\mathbf{r}, t; \boldsymbol{\mu})}{dt} + A(\mathbf{r}, t; \boldsymbol{\mu})\theta(\mathbf{r}, t; \boldsymbol{\mu}) + F(\theta(\mathbf{r}, t; \boldsymbol{\mu}), \mathbf{r}, t; \boldsymbol{\mu}) = S(\mathbf{r}, t; \boldsymbol{\mu}), \quad \mathbf{r} \in \Omega, \quad (1)$$

where  $\theta$  is an arbitrary solution variable,  $A$  a linear operator,  $F$  a nonlinear function, and  $S$  a source term. Note that the governing laws describing the behavior of a nuclear reactor can be, in fact, cast into this general form. Furthermore, we see that all of the operators and source terms (and therefore the solution as well) may depend on space, time, and a vector of model parameters denoted by  $\boldsymbol{\mu}$ . For the sake of conciseness, and the fact that they are strongly case-dependent, the initial and boundary conditions of Eq. (1) are not discussed in detail. We refer the reader to Section 4.1 for details about these.

The first step in the training phase is the generation of a Full-Order Model (FOM). This involves the discretization of Eq. (1) in space, time and in some cases other variables as well. In this work, we employ a cell-centered finite volume approach for the discretization in space, which entails splitting domain  $\Omega$  into  $N$  cells and assuming that the solution field is constant within the cells and on the cell boundaries. Then, the governing equations are integrated to obtain a system where the only unknowns are the field values at the cell centers. By applying the finite volume method to Eq. (1) we arrive to the following discretized form:

$$\mathbf{M}_{\Omega} \frac{d\boldsymbol{\theta}(t; \boldsymbol{\mu})}{dt} + \mathbf{A}(t; \boldsymbol{\mu})\boldsymbol{\theta}(t; \boldsymbol{\mu}) + \mathbf{F}(\boldsymbol{\theta}(t; \boldsymbol{\mu}), t; \boldsymbol{\mu}) = \mathbf{S}(t; \boldsymbol{\mu}), \quad (2)$$

where  $\mathbf{M}_{\Omega}$  is a diagonal mass matrix which contains the cell volumes,  $\boldsymbol{\theta}$  the solution vector,  $\mathbf{A}$  the discretized linear operator, while  $\mathbf{F}$  and  $\mathbf{S}$  are the discretized nonlinear function and source terms, respectively. For vector-valued problems (such as the fluid momentum equation),  $\mathbf{M}_{\Omega}$  is a block-diagonal matrix.

Then, the offline phase continues with learning about the time- and parameter-dependent solution manifold. To do this, we first evaluate the FOM with different model parameter values. In this process, several

instances of the fields of interest are saved at different times and model parameter values. This process is often referred to as the method of snapshots (Sirovich, 1987). For the example case presented above, a snapshot is a time-parameter realization of the  $\theta(t; \mu)$  solution vector. Additionally, for reasons discussed later, we take snapshots of the evaluated nonlinear function ( $F(\theta(t; \mu); t; \mu)$ ) as well. The snapshots are organized in corresponding snapshot matrices:

$$\mathbf{R}_\theta = [\theta(t_1; \mu_1), \theta(t_2; \mu_1), \dots, \theta(t_{N_\tau-1}; \mu_{N_\mu}), \theta(t_{N_\tau}; \mu_{N_\mu})] \quad (3a)$$

and

$$\mathbf{R}_F = [F(\theta(t_1; \mu_1), t_1; \mu_1), \dots, F(\theta(t_{N_\tau}; \mu_{N_\mu}), t_{N_\tau}; \mu_{N_\mu})]. \quad (3b)$$

We note that for transient problems,  $N_\tau$  snapshots are taken throughout each transient with  $N_\mu$  different model parameters. Therefore, the total number of snapshots can be computed by  $N_s = N_\tau \times N_\mu$  for transient and  $N_s = N_\mu$  for steady-state problems, respectively.

Next, the dominant manifold characteristics are extracted from the snapshots. For a POD-RB technique, the dominant characteristics denote global spatial basis functions which are used for the approximation of the solution and the nonlinear term as follows:

$$\theta(t; \mu) \approx \sum_{i=1}^{r_\theta} \psi_i^\theta c_i^\theta(t; \mu) = \Psi^\theta c^\theta \quad (4)$$

$$F(\theta(t_{N_\tau}; \mu_{N_\mu})) \approx \sum_{i=1}^{r_F} \psi_i^F c_i^F(c^\theta(t; \mu), t; \mu) = \Psi^F c^F. \quad (5)$$

This means the fields of interest are approximated as the linear combination of space-dependent global basis vectors ( $\psi$ ) with the expansion coefficients denoted by  $c$ . Since each basis vector corresponds to the finite volume representation of an actual spatial basis function  $\psi$ , the two terms are used interchangeably in this work. The basis functions for the reduced-basis approximation are determined by applying Proper Orthogonal Decomposition (POD) (Pinnau, 2008; Pearson, 1901; Sirovich, 1987) to the snapshot matrices. This results in a set of basis functions which span a subspace closest to the snapshot subspace in an  $L^2$  sense. It can be proven that these basis functions can be computed using the constrained Singular Value Decomposition (SVD) (Abdi, 2007) of the snapshot matrix:

$$\mathbf{R}_\theta = \Psi^\theta \mathbf{W}^\theta \mathbf{V}^\theta, \quad \text{such that} \quad \Psi^{\theta,T} \mathbf{M}_\Omega \Psi = \mathbf{I}, \quad (6)$$

where  $\Psi^\theta$  and  $\mathbf{V}^\theta$  are the left- and right-singular vectors, while  $\mathbf{W}^\theta$  is a diagonal matrix containing the singular values  $\omega_i^\theta$ . The same process is applied to generate the basis functions for the nonlinear function term as well. In this work, we determine the number of required basis functions for the fields of interest ( $r_\theta$  and  $r_F$ ) by keeping only  $r$  modes such that an information (or energy) retention criterion is satisfied:

$$r_\theta = \arg \min_{1 \leq r \leq N_s} \left( \frac{\sum_{k=1}^r \omega_k^{\theta,2}}{\sum_{k=1}^{N_s} \omega_k^{\theta,2}} > 1 - \tau \right), \quad (7)$$

where  $\tau$  is an energy retention limit. For more information about the generation of basis functions we refer the interested reader to Lorenzi et al. (2016), German et al. (2020) and German and Ragusa (2019).

Once the basis functions of the reduced subspace are determined, the offline phase proceeds to the next step which is the generation of reduced operators. To generate these reduce operators, we first plug the reduced-basis approximates Eqs. (4)–(5) into the FOM (Eq. (2)) and use a Galerkin projection with  $\Psi^\theta$  as trial functions to obtain a well-posed system:

$$\frac{\partial c^\theta(t; \mu)}{\partial t} + \Psi^{\theta,T} \mathbf{A}(t; \mu) \Psi^\theta c^\theta(t; \mu) + \Psi^{\theta,T} \mathbf{F}(\Psi^\theta c^\theta(\mu, t), t; \mu) = \Psi^{\theta,T} \mathbf{S}(t; \mu), \quad (8)$$

This can be further simplified by introducing the reduced operator  $\mathbf{A}^r(t; \mu) = \Psi^{\theta,T} \mathbf{A}(t; \mu) \Psi^\theta$  and the reduced vectors  $\mathbf{S}^r(t; \mu) = \Psi^{\theta,T} \mathbf{S}(t; \mu)$ :

$$\frac{\partial c^\theta(t; \mu)}{\partial t} + \mathbf{A}^r(t; \mu) c^\theta(t; \mu) + \Psi^{\theta,T} \mathbf{F}(\Psi^\theta c^\theta(t; \mu), t; \mu) = \mathbf{S}^r(t; \mu). \quad (9)$$

It is clear at this point that the only unknowns in the system are the expansion coefficients, elements of the reduced solution vectors  $c^\theta(\mu, t)$ , which means that the number of unknowns is reduced from  $N$  for the full-order model to  $r_\theta \ll N$  for the reduced-order model, hence offering a potentially large reduction in simulation time. However, solving the reduced system as written might not necessarily be faster than solving the FOM because of the following two considerations:

1. If operator  $\mathbf{A}$  and source term  $\mathbf{S}$  have a general dependence on time and model parameters, the corresponding reduced terms have to be created from the full-order ones at every time step or new parameter value. Having to create full-order operators might yield negligible savings in computational time. However, if the reduced terms can be expressed as the sum of products of only space dependent operators and time- and parameter-dependent scalar functions (i.e., when using an affine decomposition), then the space-dependent constituent operators can be reduced one-by-one during the offline phase and the online ROM phase will only involve the manipulation of small dense matrices and vectors.
2. The nonlinear term has to be evaluated at each nonlinear iteration. This operation also scales with  $N$  (also a full-order operation), which may also limit the ROM computational speedup. For this reason, the Discrete Empirical Interpolation Method (DEIM) (Chaturantabud and Sorensen, 2010) is used to interpolate  $\mathbf{F}$  using basis vectors  $\Psi^F$  as:

$$\mathbf{F}(\Psi^\theta c^\theta(t; \mu), t; \mu) \approx \Psi^F c^F(c^\theta(t; \mu), t; \mu) \quad (10)$$

where the interpolation coefficients ( $c^F$ ) can be determined using  $c^\theta$  by collocation at  $r_F$  rows of the nonlinear vector. For more information on the utilization of DEIM in the developed framework, see German et al. (2019, 2021). Certain nonlinear terms, e.g., polynomial-like nonlinearities (such as the advection terms in the fluid momentum equations), do not require the utilization of DEIM, as it is enough to compute a higher-order ROM tensor to restore computational efficiency. This is shown in Stabile and Rozza (2018), Lorenzi et al. (2016), German et al. (2021) and German (2021).

We note that the training phase of the procedure is computationally expensive because it requires the repeated solution of the FOM and the computation of the reduced operators. This is, however, a one-time investment which can be justified if the original task requires a considerably larger computational effort than the generation of the ROM. Multi-query problems such as uncertainty quantification or design optimization are good application examples for ROMs, since they would require repeated evaluations of the FOM otherwise. In these scenarios, ROMs can be trained using a fraction of the FOM evaluations and the multi-query problem can then be addressed using the ROMs as emulators.

Once the training phase is concluded, the process continues with the online or evaluation phase. The first step in the online phase is the assembly of the ROM from the reduced operators precomputed in the offline phase. If the operators have an affine dependence on the parameters and the nonlinearities are resolved using either DEIM or a polynomial approach, this step only involves operations with small dense matrices and vectors. This makes the online phase extremely cheap in terms of computational time. Once the ROM system of equations is assembled, it can be solved to obtain the  $c^\theta$  expansion coefficients. This requires the temporal discretization of the ODEs for the expansion coefficients (see Eq. (9)) and the solution of the linearized problem at every time step until convergence. With the reduced equations solved, the expansion coefficients are used to evaluate different Quantities of Interest (QoIs). This can be done either

directly if the QoIs have affine dependence on the parameters, time, and expansion coefficients (e.g., point values, averages of the solution) or indirectly through the reconstruction of the reduced-basis approximate (e.g.,  $L^2$  errors compared to a field). The following sections discuss some Molten-Salt-Reactor-specific details of the above MOR procedure.

### 3. Governing equations for liquid-fuel Molten Salt Reactors

The simulation of liquid-fuel MSR requires the solution of a system of coupled partial differential equations describing fluid dynamics, heat transfer and neutronics phenomena. In this work, the incompressible porous medium Reynolds Averaged Navier–Stokes (RANS) equations are solved to obtain the velocity and pressure fields in the system (Fiorina et al., 2015; German et al., 2021). This approach homogenizes complex solid structures into porous-medium zones and handles the fluid–structure interactions with semi-empirical correlation functions:

$$\nabla \cdot \rho \mathbf{u}_D = 0, \quad \mathbf{r} \in \Omega, \quad (11)$$

$$\begin{aligned} \frac{\partial \rho \mathbf{u}_D}{\partial t} + \frac{1}{\gamma} \nabla \cdot (\rho \mathbf{u}_D \otimes \mathbf{u}_D) = \nabla \cdot \left( (\eta + \eta_t) \left[ \nabla \mathbf{u}_D + (\nabla \mathbf{u}_D)^T \right] \right) - \gamma \nabla p \\ + \gamma F_p + \gamma F_{fr} + \gamma \beta_{th} \rho g \cdot \mathbf{r} \nabla T, \quad \mathbf{r} \in \Omega. \end{aligned} \quad (12)$$

where  $\mathbf{u}_D = \mathbf{u}_D(\mathbf{r}, t) = \mathbf{u}(\mathbf{r}, t)\gamma(\mathbf{r})$  denotes the Reynolds-averaged Darcy velocity vector field, which is computed using the real velocity field  $\mathbf{u}(\mathbf{r}, t)$  and the volume fraction of the fluid in the porous medium zones  $\gamma(\mathbf{r})$ . Note, if  $\gamma = 1$  (clear fluid zones), the formulation devolves into the original form of the RANS equations. Furthermore,  $p = p(\mathbf{r}, t)$  denotes the Reynolds-averaged corrected pressure field,  $T = T(\mathbf{r}, t)$  the Reynolds-averaged temperature field, while  $\eta$  is the molecular dynamic viscosity,  $\rho$  the density, and  $\beta_{th}$  the thermal expansion coefficient. We consider  $\rho$ ,  $\eta$  and  $\beta_{th}$  to be constants. For the derivation of the corrected pressure in terms of the total pressure, hydrostatic pressure, and temperature, we refer the reader to German et al. (2021). The last term on the right hand side of Eq. 12 describes the buoyancy effect using a Boussinesq approximation with  $g$  denoting the gravitational acceleration.  $F_p = F_p(\mathbf{r}, t)$  and  $F_{fr} = F_{fr}(\mathbf{r}, t, \mathbf{u})$  are volumetric forces describing the actions of a pump ( $F_p$ ) and the flow resistance of the homogenized structural elements ( $F_{fr}$ ). In this work, the turbulent viscosity,  $\eta_t$ , is computed using a porous medium  $k - \epsilon$  model (Fiorina et al., 2015). Lastly, we note that only homogeneous Dirichlet boundary conditions are considered for the velocity ( $\mathbf{u}_D = \mathbf{0}$ ) and homogeneous Neumann conditions are used for the corrected pressure ( $\nabla p \cdot \mathbf{n} = 0$ ). Physically, this corresponds to a closed-loop system.

To determine the Reynolds-averaged temperature field in the system, we solve the porous-medium enthalpy equation (German et al., 2021), which is derived from the porous-medium total energy equation in Fiorina et al. (2015) with the assumption that the kinetic energy of the circulated molten salt is negligible compared to its internal energy/enthalpy:

$$\begin{aligned} \frac{\partial \gamma \rho c_p T}{\partial t} + \nabla \cdot (\mathbf{u}_D \rho c_p T) = \nabla \cdot \left( \gamma \left[ k_l + c_p \alpha_l \right] \nabla T \right) - h A_V (T - T_{ext}) \\ + \gamma \sum_{g=1}^{G_e} \Sigma_{p,g} \phi_g, \quad \mathbf{r} \in \Omega \end{aligned} \quad (13)$$

where  $k_l$  and  $c_p$  denote the thermal conductivity and specific heat of the fluid. In this work, these material properties are considered to be constant.  $h$  is the heat transfer coefficient,  $A_V$  the volumetric surface, and  $T_{ext}$  the temperature of the homogenized structural element. The last term on the right hand side of Eq. (13) describes the volumetric fission power deposition in the fluid (liquid fuel). Mixing effects from the turbulence are taken into account using  $\alpha_t = \frac{\eta_t}{Pr_t}$  turbulent diffusivity with turbulent Prandtl number  $Pr_t$ . Lastly, we note that only homogeneous Neumann boundary conditions ( $\nabla T \cdot \mathbf{n} = 0$ ) are considered for temperature with the assumption that the nuclear systems are properly insulated.

Based on prior works, e.g., Fiorina et al. (2012) and Tano Retamalos (2018), we assume that the neutronics behavior of the system can be modeled using the multi-group diffusion equations (Duderstadt and Hamilton, 1976):

$$\begin{aligned} \frac{1}{v_g} \frac{\partial \phi_g}{\partial t} = \nabla \cdot [D_g \nabla \phi_g] - \Sigma_{t,g} \phi_g + \frac{(1-\beta) \chi_{p,g}}{k_{eff}} \sum_{g'=1}^{G_e} v_{g'} \Sigma_{f,g'} \phi_{g'} \\ + \sum_{g'=1}^{G_e} \Sigma_{s,g' \rightarrow g} \phi_{g'} + \chi_{d,g} \sum_{i=1}^{G_d} \lambda_i \gamma C_i^*, \quad \mathbf{r} \in \Omega, \quad g \in [1, \dots, G_e], \end{aligned} \quad (14)$$

where  $v_g$  denotes the velocity of neutrons,  $\phi_g$  the scalar flux,  $D_g$  the diffusion coefficient,  $v_g$  the fission neutron yield, while  $\Sigma_{t,g}$  and  $\Sigma_{f,g}$  the macroscopic total and fission cross sections in energy group  $g = 1, \dots, G_e$ . Furthermore,  $\beta$  is the total delayed neutron fraction,  $\chi_{p,g}$  the prompt neutron spectrum,  $\chi_{d,g}$  the delayed neutron spectrum and  $\Sigma_{s,g' \rightarrow g}$  is the macroscopic scattering cross section from energy group  $g'$  to  $g$ . The last term on the right hand side of Eq. (14) expresses a delayed neutron source and contains the corrected delayed neutron precursor concentrations,  $C_i^*$ , together with the corresponding decay constants  $\lambda_i$ . Therefore, additional equations are needed for the balance of delayed neutron precursors which can be expressed as:

$$\begin{aligned} \frac{\partial \gamma C_i^*}{\partial t} + \nabla \cdot [\mathbf{u}_D C_i^*] = \nabla \cdot \left( \left[ \frac{\alpha_l}{\rho} + \frac{\alpha_t}{\rho} \right] \nabla C_i^* \right) \\ + \frac{\beta_i}{k_{eff}} \sum_{g'=1}^{G_e} v_{g'} \Sigma_{f,g'} \phi_{g'} - \lambda_i \gamma C_i^*, \quad \mathbf{r} \in \Omega, \quad i \in [0, \dots, G_d] \end{aligned} \quad (15)$$

where  $C_i^* = \frac{C_i}{\gamma}$  is the corrected precursor concentration,  $\alpha_l$  and  $\alpha_t$  are the laminar and turbulent mass diffusivity of the precursors, respectively, and  $\beta_i$  the delayed neutron fraction in group  $i$ .  $k_{eff}$  denotes the effective multiplication factor which is the largest eigenvalue of the steady-state system (without time derivatives). It is important to mention that the group constants in Eqs. (14)–(15) depend on the temperature and the density of the molten fuel salt:

$$\Sigma_g = \Sigma_g(T, \rho(T)), \quad \text{with} \quad \rho(T) = \rho_{ref} (1 + \beta_{th} [T - T_{ref}]) \quad (16)$$

meaning that, for the neutronics subproblem, the density of the fluid is assumed to be a linear function of the temperature. Homogeneous Robin boundary conditions are used for the group fluxes ( $-D_i \nabla \phi_g \cdot \mathbf{n} = \gamma_i \phi_g$ ), which correspond to vacuum or albedo conditions for the diffusion approximation. At the same time, simulating a closed-loop system, homogeneous Neumann condition is used for the corrected precursor concentrations ( $\nabla C_i^* \cdot \mathbf{n} = 0$ ).

Due to the fact that the delayed neutron precursors move within the core, one of the most important operational parameter for a MSRs is the effective delayed neutron fraction. The computation of this quantity of interest (QoI), however, requires the solution of the adjoint neutronics problem for the neutron and corrected precursor importance fields ( $\phi_g^\dagger$  and  $C_i^{*\dagger}$ ). These equations can be written as (Aufiero et al., 2014; Shi and Fratoni, 2021):

$$\begin{aligned} -\nabla \cdot [D \nabla \phi^\dagger] + \Sigma_t \phi^\dagger - \sum_{g'=1}^{G_e} \Sigma_{g \rightarrow g'} \phi_{g'}^\dagger = \frac{(1-\beta) v_g \Sigma_{f,g}}{k_{eff}} \sum_{g'=1}^{G_e} \chi_{p,g'} \phi_{g'}^\dagger \\ + \frac{v \Sigma_f}{k_{eff}} \sum_{i=1}^{G_d} \beta_i \gamma C_i^{*\dagger} \end{aligned} \quad (17)$$

$$\nabla \cdot (-\mathbf{u}_D C_i^{*\dagger}) - \nabla \cdot \left( \left[ \frac{\alpha_l}{\rho} + \frac{\alpha_t}{\rho} \right] \nabla C_i^{*\dagger} \right) + \lambda_i \gamma C_i^{*\dagger} = \lambda_i \sum_{g'=1}^{G_e} \chi_{d,g'} \phi_{g'}^\dagger. \quad (18)$$

Using the neutron and precursor importances together with the scalar fluxes and precursor concentrations from the forward problem, the effective delayed neutron fraction in group  $i$  can be computed as (Aufiero

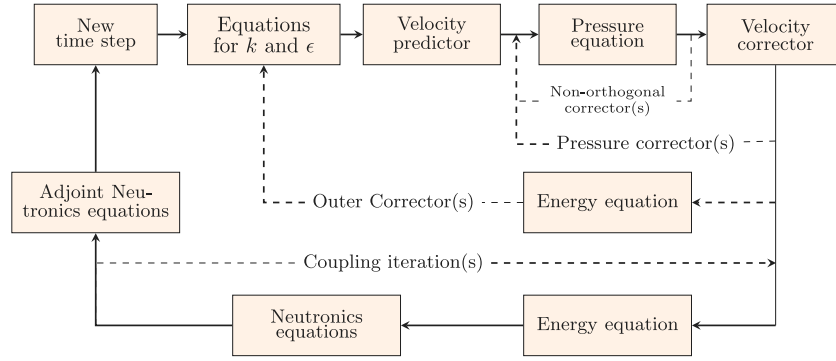


Fig. 2. The solution algorithm for the Full-Order Models. Derived from the work in Fiorina et al. (2015) by the application of the incompressibility constrain and the addition of the adjoint neutronics solver. (solid lines — the default coupling, dashed lines — possible inner iterations).

et al., 2014; Shi and Fratoni, 2021):

$$\beta_{\text{eff},i} = \frac{\sum_{g=1}^{G_e} \int_{\Omega} \phi_g^\dagger \chi_{d,i} \lambda_i C_i d\Omega}{\sum_{g=1}^{G_e} \int_{\Omega} \phi_g^\dagger \left( \chi_{d,g} \sum_{j=0}^{G_d} \lambda_j C_j + \chi_{p,g} \sum_{g'=1}^{G_e} \nu \Sigma_{f,g'} \phi_{g'} \right) d\Omega}, \quad (19)$$

and the total effective delayed neutron fraction can be computed as the sum of the group-wise contributions.

Lastly, we recall that the governing equations are considered to be parametric in a sense that the solutions depend on input parameters like group constants, material properties, initial and boundary conditions, to name a few. We denote the vector containing the model parameters by  $\mu = [\mu_1, \mu_2, \dots, \mu_d]^T$ , where it is assumed that there are altogether  $d$  model parameters in the system.

#### 4. Training or offline phase

##### 4.1. Generation of the Full-Order Models (FOMs)

The offline phase begins with the discretization of the governing equations which yields a higher-fidelity numerical model (FOM). For this task, GeN-Foam<sup>2</sup> (General Nuclear Foam) (Fiorina et al., 2015), an OpenFOAM<sup>®</sup>-based (Jasak et al., 2007) multiphysics finite volume framework has been utilized since it provides advanced capabilities for the simulation of MSRs. The system of governing equations is solved using a fixed-point iteration in a segregated manner. The flow chart of the iteration scheme between the segregated subproblems is presented in Fig. 2. Steady-state simulations use the same scheme and they are iterated until convergence using relaxed pseudo-time stepping.

An important detail of the FOM is the handling of the temperature- and density-dependent group constants. For this, in GeN-Foam, three libraries are prepared (Fiorina et al., 2016): one with a reference temperature and density ( $T_{\text{ref}}, \rho_{\text{ref}} = \rho(T_{\text{ref}})$ ), another one with perturbed temperature ( $T_{\text{pert}}, \rho_{\text{ref}}$ ) and the last with perturbed density ( $T_{\text{ref}}, \rho_{\text{pert}}$ ). Then, the following feedback coefficients are computed:

$$\delta_{FT} = \frac{\Sigma(T_{\text{ref}}, \rho_{\text{ref}}) - \Sigma(T_{\text{pert}}, \rho_{\text{ref}})}{T_{\text{ref}}^{\text{aux}} - T_{\text{pert}}^{\text{aux}}} \quad \text{and} \quad \delta_{FD} = \frac{\Sigma(T_{\text{ref}}, \rho_{\text{ref}}) - \Sigma(T_{\text{ref}}, \rho_{\text{pert}})}{\rho_{\text{ref}} - \rho_{\text{pert}}}, \quad (20)$$

where  $\Sigma$  is an arbitrary group constant and  $T^{\text{aux}} = \sqrt{T}$  for thermal spectrum reactors, while  $T^{\text{aux}} = \ln(T)$  for fast spectrum reactors. Using these coefficients and the assumption that the density is a linear function of the temperature (see Eq. (16)), we can express the temperature-dependent group constant as:

$$\Sigma(T) \approx \Sigma(T_{\text{ref}}, \rho_{\text{ref}}) + \delta_{FT} (T^{\text{aux}} - T_{\text{ref}}^{\text{aux}}) + \delta_{FD} \beta_{th} \rho_{\text{ref}} (T - T_{\text{ref}}). \quad (21)$$

<sup>2</sup> GeN-Foam repository: <https://gitlab.com/foam-for-nuclear/GeN-Foam>, Accessed: 12/08/2020.

##### 4.2. Learning the solution manifold

The time- and parameter-dependent solution manifold is explored using the method of snapshots. This involves exercising the FOM with  $N_\mu$  different model parameter combinations and saving the fields of interest. For parametric transients, the solution fields are captured at  $N_\tau$  time instances yielding  $N_s = N_\tau \times N_\mu$  snapshots. For steady-state problems, only the converged solutions are saved, therefore  $N_s = N_\mu$ . The snapshots are saved directly in a snapshot matrix:

$$\mathbf{R}_X = [\mathbf{X}(t_1, \mu_1) \dots \mathbf{X}(t_{N_\tau}, \mu_{N_\mu})] \quad (22)$$

where  $X$  can be any field from the following set:  $\{\phi_g, \phi_g^\dagger, C_i^*, C_i^{\dagger,*}, \mathbf{u}_D, p, \mathbf{F}_{fr}^z, T, T^{\text{aux}}, \eta_t, \alpha_t\}$  with  $g = 1, \dots, G_e$ ,  $i = 1, \dots, G_d$  and  $z = 1, \dots, N_z$  denoting the energy group, precursor group and porous medium zone indices. The importance of capturing snapshots for the auxiliary temperature fields and for flow resistance in zone  $z$  is discussed later in detail.

Next, we assume that these solution fields can be accurately approximated as the linear combination of  $r_X$  global basis functions:

$$\mathbf{X}(t, \mu) \approx \sum_{i=1}^{r_X} \psi_i^X c_i^X(t; \mu), \quad (23)$$

where the  $c_i$  expansion coefficients describe the evolution of the field in time and parameter space. We use Proper Orthogonal Decomposition (POD), discussed in Section 2, for the generation of the global basis functions, with three exceptions in case the user chooses to reduce the fluid dynamics equations using a one-equation technique. In general, GeN-ROM is capable of generating one- and two-equation fluid dynamics ROMs. The one-equation ROM approach has been introduced in Lorenzi et al. (2016) for laminar and turbulent clean fluid flows and is based on the reduction of the momentum equation alone with additional approximations regarding the pressure and eddy viscosity fields. Namely, that the coefficients of the pressure and eddy viscosity are the same as the those of the velocity:  $c^{u_D} = c^p = c^{\eta_t}$ . This entails that the basis functions of the mentioned fields need to be generated in a slightly different manner. For more details on the two fluid dynamics ROMs implemented in GeN-ROM, including the differences in the computation of the corresponding basis functions, the interested reader is referred to German et al. (2020).

##### 4.3. Generation of reduced operators

To obtain the reduced operators, we seek our fields of interest as a linear combination of the learned global basis vectors, as shown in Eq. (23), and use these expansions in the governing equations. Then, the equations are projected using the same basis functions (Galerkin projection) of the corresponding solution fields. In the following subsections we present only the final forms of the reduced equations.

For a step-by-step example of the derivations using the fluid dynamics equations, see [Appendix A](#).

#### 4.3.1. Reduced fluid dynamics equations

We plug the reduced-basis approximates of the fields of interest into Eqs. 11–12 and project the momentum and continuity equations using the velocity and pressure basis functions. As shown in [German et al. \(2021\)](#), the reduced fluid dynamics equations can be written in the following form:

$$\rho \mathbf{G} \mathbf{c}^{u_D} = 0, \quad (24)$$

$$\begin{aligned} & \rho \mathbf{M} \dot{\mathbf{c}}^{u_D} + \rho \mathbf{c}^{u_D, T} \overline{\overline{\mathbf{C}}} \mathbf{c}^{u_D} - \mathbf{c}^{\eta, T} \overline{\overline{\mathbf{T}}} \mathbf{c}^{u_D} - \eta \mathbf{D} \mathbf{c}^{u_D} + \mathbf{P} \mathbf{c}^p \\ & - \sum_{z=1}^{N_z} \left( |F_{p,z}| \mathbf{S}_{p,z} - \mathbf{S}_{f,r,z} \mathbf{c}_z^{F_{fr}} \right) - \rho \beta_{th} \mathbf{A} \mathbf{c}^T = 0, \end{aligned} \quad (25)$$

where the entries of the reduced operators can be expressed using a selection operator,  $\delta_z(\mathbf{r})$ , which returns 1 if  $\mathbf{r}$  is in porous medium zone  $z$  and 0 otherwise:

$$\begin{aligned} \mathbf{M}_{i,j} &= \left\langle \psi_i^{u_D}, \psi_j^{u_D} \right\rangle_{\Omega} \\ \overline{\overline{\mathbf{C}}}_{i,j,k} &= \left\langle \psi_j^{u_D}, \frac{1}{\gamma} \nabla \cdot (\psi_i^{u_D} \otimes \psi_k^{u_D}) \right\rangle_{\Omega} \\ \mathbf{D}_{i,j} &= \left\langle \psi_i^{u_D}, \nabla \cdot \left[ \nabla \psi_j^{u_D} + (\nabla \psi_j^{u_D})^T \right] \right\rangle_{\Omega} \\ \mathbf{P}_{i,j} &= \left\langle \psi_i^{u_D}, \gamma \nabla \psi_j^p \right\rangle_{\Omega} \\ \mathbf{S}_{p,z,i} &= \left\langle \psi_i^{u_D}, \gamma \frac{\delta_z(\mathbf{r}) \mathbf{F}_{p,z}}{|F_{p,z}|} \right\rangle_{\Omega} \\ \mathbf{G}_{i,j} &= \left\langle \psi_i^p, \nabla \cdot \psi_j^{u_D} \right\rangle_{\Omega} \\ \overline{\overline{\mathbf{T}}}_{i,j,k} &= \left\langle \psi_j^{u_D}, \nabla \cdot (\psi_i^{\eta} [\nabla \psi_k^{u_D} + (\nabla \psi_k^{u_D})^T]) \right\rangle_{\Omega} \\ \mathbf{S}_{f,r,z,i,j} &= \left\langle \psi_i^{u_D}, \delta_z(\mathbf{r}) \psi_j^{F_{fr,z}} \right\rangle_{\Omega} \\ \mathbf{A}_{i,j} &= \left\langle \psi_i^{u_D}, \gamma \mathbf{g} \cdot \mathbf{r} \nabla \psi_j^T \right\rangle_{\Omega}, \end{aligned}$$

where the  $\langle \cdot, \cdot \rangle_{\Omega}$  denotes a volumetric inner product. We note that this reduced equation is not stable due to the violation of the Ladyzhenskaya–Babuska–Brezzi (LBB) condition ([Gerner and Veroy, 2012](#); [Ballarin et al., 2015](#)). Therefore, two techniques are implemented in GeN-ROM: a supremizer stabilization and a physics-based approximation that yields a one-equation model. For more information on these techniques, the interested reader is referred to [Ballarin et al. \(2015\)](#), [Stabile and Rozza \(2018\)](#), [Lorenzi et al. \(2016, 2017\)](#), [German et al. \(2020\)](#) and [German et al. \(2021\)](#). Furthermore, the coefficients of the flow resistances ( $\mathbf{c}_z^{F_{fr}}$ ) in terms of the velocity coefficients are determined using the Discrete Empirical Interpolation Method (DEIM) based technique discussed in [German et al. \(2021\)](#). For turbulent fluid flows, the coefficients of the eddy viscosity/diffusivity are determined depending on what stabilization technique is used for the fluid dynamics ROM. If a supremizer stabilization is chosen, a non-intrusive ROM approach involving Radial Basis Function (RBF) interpolation is utilized. This method has been applied to clean fluid flows ([Hijazi et al., 2018, 2019](#)) and the version used in GeN-ROM is described in [German et al. \(2020, 2021\)](#) in detail. On the other hand, if a one-equation fluid ROM is chosen, the coefficients of the eddy viscosity are approximated with the coefficients of the velocity ( $\mathbf{c}^{u_D} = \mathbf{c}^{\eta}$ ) which is considered to be a physics based approach ([Lorenzi et al., 2016, 2017](#)). Lastly, it must be mentioned that the expression above assumes that a homogeneous Dirichlet and Neumann conditions are used for the velocity and pressure fields, respectively. For examples with heterogeneous boundary conditions and their enforcement at reduced-order level, see [Stabile and Rozza \(2018\)](#), [Stabile et al. \(2017\)](#), [Lorenzi et al. \(2016\)](#) and [German et al. \(2020\)](#) and [Appendix B](#). The reduced fluid dynamics equations are then solved for the expansion coefficients of the pressure and velocity

while keeping the temperature coefficients of the other variables fixed in the nonlinear iteration.

#### 4.3.2. Reduced energy equation

Following [German et al. \(2021\)](#), the porous-medium enthalpy equations are reduced by plugging the reduced-basis approximations into Eq. (13) and projecting using the basis function of the temperature:

$$\begin{aligned} & \rho c_p \mathbf{M}_{\gamma} \dot{\mathbf{c}}^T + \rho c_p \mathbf{c}^{u_D, T} \overline{\overline{\mathbf{A}}} \mathbf{c}^T - k_l \mathbf{K}_l \mathbf{c}^T - \mathbf{c}^{\alpha, T} c_p \overline{\overline{\mathbf{K}}}_l \mathbf{c}^T = \\ & - \left( \sum_{z=1}^{N_z} h^z A_V^z \mathbf{M}^z \right) \mathbf{c}^T + \left( \sum_{z=1}^{N_z} h^z A_V^z T_{\text{ext}} s_h^z \right) \\ & + \sum_{g=1}^{G_e} \left( \sum_{z=1}^{N_z} \Sigma_{p,g}^z \mathbf{S}_{p,g}^z \right) \mathbf{c}^{\phi_g}, \end{aligned} \quad (26)$$

where the entries of the reduced operators can be computed as

$$\begin{aligned} (\mathbf{M}_{\gamma})_{i,j} &= \left\langle \psi_i^T, \gamma \psi_j^T \right\rangle_{\Omega}, \\ (\overline{\overline{\mathbf{A}}})_{i,j,k} &= \left\langle \psi_i^T, \nabla \cdot (\psi_k^{u_D} \psi_j^T) \right\rangle_{\Omega}, \\ (\mathbf{K}_l)_{i,j} &= \left\langle \psi_i^T, \nabla \cdot (\gamma \nabla \psi_j^T) \right\rangle_{\Omega}, \\ (\overline{\overline{\mathbf{K}}}_l)_{i,j,k} &= \left\langle \psi_i^T, \nabla \cdot (\gamma \psi_k^{\alpha} \nabla \psi_j^T) \right\rangle_{\Omega}, \\ (\mathbf{M}^z)_{i,j} &= \left\langle \psi_i^T, \delta_z(\mathbf{r}) \psi_j^T \right\rangle_{\Omega}, \\ (s_h^z)_i &= \left\langle \psi_i^T, \delta_z(\mathbf{r}) \right\rangle_{\Omega}, \\ (\mathbf{S}_{p,g}^z)_{i,j} &= \left\langle \psi_i^T, \delta_z(\mathbf{r}) \gamma \psi_j^{\phi_g} \right\rangle_{\Omega}. \end{aligned}$$

This equation is solved for the expansion coefficients of the temperature, while keeping the coefficients of the velocity, eddy diffusivity and group fluxes fixed.

#### 4.3.3. Reduced neutronics equations

A group-wise reduction is chosen in this work, since it has been proven to be more robust, especially for eigenvalue problems ([German and Ragusa, 2019](#)). The reduced neutron balance equation can be written as follows:

$$\begin{aligned} & \left( \sum_{z=1}^{N_z} \frac{1}{V_g^z} \mathbf{M}_{g,g}^z \right) \dot{\mathbf{c}}^{\phi_g} + \left( \sum_{z=1}^{N_z} -D_g^z \mathbf{K}_g^z + \Sigma_{t,g}^z \mathbf{M}_{g,g}^z \right) \mathbf{c}^{\phi_g} \\ & = \frac{1}{k_{\text{eff}}^r} \sum_{g'=1}^{G_e} \left( \sum_{z=1}^{N_z} (1 - \beta^z) \chi_{p,g}^z \nu_{g'}^z \Sigma_{f,g'}^z \mathbf{M}_{g,g'}^z \right) \mathbf{c}^{\phi_{g'}} \\ & + \sum_{g'=1}^{G_e} \left( \sum_{z=1}^{N_z} \Sigma_{s,g' \rightarrow g}^z \mathbf{M}_{g,g'}^z \right) \mathbf{c}^{\phi_{g'}} + \sum_{i=1}^{G_d} \left( \sum_{z=1}^{N_z} \chi_{d,g}^z \lambda_i^z \mathbf{P}_{g,i}^z \right) \mathbf{c}^{C_i^e} \end{aligned} \quad (27)$$

where the elements of the reduced operators can be computed using the selection operator  $\delta_z(\mathbf{r})$  as:

$$\begin{aligned} (\mathbf{M}_{g,g'})_{i,j} &= \left\langle \psi_i^{\phi_g}, \delta_z(\mathbf{r}) \psi_j^{\phi_{g'}} \right\rangle_{\Omega}, \\ (\mathbf{K}_g^z)_{i,j} &= \left\langle \psi_i^{\phi_g}, \nabla \cdot (\delta_z(\mathbf{r}) \nabla \psi_j^{\phi_g}) \right\rangle_{\Omega}, \\ (\mathbf{P}_{g,k}^z)_{i,j} &= \left\langle \psi_i^{\phi_g}, \delta_z(\mathbf{r}) \gamma \psi_j^{C_k^e} \right\rangle_{\Omega}. \end{aligned}$$

We note that the expressions above do not show the treatment of boundary conditions. For a detailed derivation and explanation of the handling of boundary conditions, we refer the reader to [Appendix B](#). In case when the temperature-dependent cross sections need to be accounted for, every term in the neutronics and enthalpy equation involving temperature-dependent group constants are treated using the Discrete Empirical Interpolation Method (DEIM) ([Chaturantabut and Sorensen, 2010](#)), which was first published in [German et al. \(2019\)](#) for the fuel temperature (Doppler) feedback and then extended in this work to include the effects of the changing salt density as well. For

more information about the developed technique, we refer the reader to [Appendix D](#).

The reduced neutron balance equations are coupled with reduced precursor concentrations which can be derived by plugging in the reduced-basis approximates into Eq. (15) and projecting by using the basis functions of the given precursor group. This results in the following ROM:

$$\begin{aligned} & \left( \sum_{z=1}^{N_z} \mathbf{M}_i^z \right) \mathbf{c}^{C_i^*} + \mathbf{c}^{u_D} \bar{\mathbf{A}}_i \mathbf{c}^{C_i^*} - \frac{\alpha_l}{\rho} \mathbf{K}_i \mathbf{c}^{C_i^*} - \mathbf{c}^{\alpha_t} \frac{1}{\rho} \bar{\mathbf{D}}_i \mathbf{c}^{C_i^*} = \\ & - \left( \sum_{z=1}^{N_z} \lambda_i^z \mathbf{M}_i^z \right) \mathbf{c}^{C_i^*} + \frac{1}{k_{\text{eff}}^r} \sum_{g'=1}^{G_e} \left( \sum_{z=1}^{N_z} \beta^z v_{g'}^z \Sigma_{f,g'}^z \mathbf{F}_{i,g'}^z \right) \mathbf{c}^{\phi_{g'}^*}, \end{aligned} \quad (28)$$

where the entries of the different reduced-order operators can be described as:

$$\begin{aligned} (\mathbf{M}_k^z)_{i,j} &= \left\langle \psi_i^{C_k^*}, \delta_z(\mathbf{r}) \gamma \psi_j^{C_k^*} \right\rangle_{\Omega}, \\ (\mathbf{F}_{k,g}^z)_{i,j} &= \left\langle \psi_i^{C_k^*}, \delta_z(\mathbf{r}) \psi_j^{\phi_g^*} \right\rangle_{\Omega}, \\ (\mathbf{K}_l)_{i,j} &= \left\langle \psi_i^{C_k^*}, \nabla^2 \psi_j^{C_k^*} \right\rangle_{\Omega}, \\ (\bar{\mathbf{A}}_i)_{i,j,k} &= \left\langle \psi_i^{C_l^*}, \nabla \cdot (\psi_k^{u_D} \psi_j^{C_l^*}) \right\rangle_{\Omega}, \\ (\bar{\mathbf{D}}_i)_{i,j,k} &= \left\langle \psi_i^{C_k^*}, \nabla \cdot (\psi_k^{\alpha_t} \nabla \psi_j^{C_k^*}) \right\rangle_{\Omega}. \end{aligned}$$

The reduced neutronics equations are solved for the expansion coefficients of the group fluxes and precursor concentrations, while keeping the coefficients of  $\mathbf{u}_D$ ,  $\alpha_t$ ,  $T$  and  $T^{\text{aux}}$  fixed.

#### 4.3.4. Reduced adjoint neutronics equations

Lastly, the adjoint equations for the neutron and precursor importances are reduced in a similar fashion. The reduced neutron importance equation can be expressed as:

$$\begin{aligned} & \left( \sum_{z=1}^{N_z} -D_g^z \mathbf{K}_g^z + \Sigma_{t,g}^z \mathbf{M}_{g,g}^z \right) \mathbf{c}^{\phi_g^\dagger} \\ &= \frac{1}{k_{\text{eff}}^r} \sum_{g'=1}^{G_e} \left( \sum_{z=1}^{N_z} (1 - \beta^z) \chi_{p,g'}^z v_g^z \Sigma_{f,g'}^z \mathbf{M}_{g,g'}^z \right) \mathbf{c}^{\phi_{g'}^\dagger} \\ &+ \sum_{g'=1}^{G_e} \left( \sum_{z=1}^{N_z} \Sigma_{s,g \rightarrow g'}^z \mathbf{M}_{g,g'}^z \right) \mathbf{c}^{\phi_{g'}^\dagger} + \frac{1}{k_{\text{eff}}^r} \sum_{i=1}^{G_d} \left( \sum_{z=1}^{N_z} v_g^z \Sigma_{f,g}^z \beta_i^z \mathbf{P}_{g,i}^z \right) \mathbf{c}^{C_i^{*,\dagger}}, \end{aligned} \quad (29)$$

with the reduced operators computed exactly like the ones introduced at Eq. (27) with replacing the basis functions of the forward group fluxes and precursor concentrations with the corresponding basis functions of the adjoint fields. For more information, see [German \(2021\)](#).

These equations are coupled to the precursor importance equations, which, after the projection using the corresponding basis functions take the following form:

$$\begin{aligned} & - \mathbf{c}^{u_D} \bar{\mathbf{A}}_i \mathbf{c}^{C_i^{*,\dagger}} - \frac{\alpha_l}{\rho} \mathbf{K}_i \mathbf{c}^{C_i^{*,\dagger}} - \mathbf{c}^{\alpha_t} \frac{1}{\rho} \bar{\mathbf{D}}_i \mathbf{c}^{C_i^{*,\dagger}} \\ &= - \left( \sum_{z=1}^{N_z} \lambda_i^z \mathbf{M}_i^z \right) \mathbf{c}^{C_i^{*,\dagger}} + \sum_{g'=1}^{G_e} \left( \sum_{z=1}^{N_z} \lambda_i^z \chi_{d,g',i}^z \mathbf{F}_{i,g'}^z \right) \mathbf{c}^{\phi_{g'}^\dagger}, \end{aligned} \quad (30)$$

where the entries of the reduced operators are computed as described at Eq. (28) with replacing the basis functions of the forward neutronics fields with those of the adjoint problem.

The adjoint reduced-order model can then be solved for the coefficients of the adjoint fields while keeping the coefficients of  $\mathbf{u}_D$ ,  $\alpha_t$ ,  $T$  and  $T_{\text{aux}}$  fixed. Once the reduced adjoint problem is solved, the expansion coefficients of the neutron importances can be used to estimate the effective delayed neutron fraction. [Appendix C](#) reviews the details of an efficient way for this process.

## 5. Evaluation or online phase

The online phase of the ROM procedure consists of three distinct steps: the assembly of the reduced system, the solution of the ROM, and the evaluation of the Quantities of Interest (QoIs). The following subsections discuss each of these steps in detail.

### 5.1. Assembly of the reduced-order equations

As already discussed in Section 2, the assembly of the reduced-order model is generally fast if the operators of the full-order model are affine in the model parameters and time. Since most of the nonlinearities in the governing equations violate this affinity, multiple Discrete Empirical Interpolation (DEIM) based strategies have been devised (see [German et al., 2021](#) and [Appendix D](#)) to restore this desired property for the flow resistance in the porous-medium momentum equations and the temperature-dependent terms in the neutronics equations.

After observing the reduced equations in Section 4.3, we conclude that the system is affine in time, group constants and parameters describing their temperature dependence, major material properties in the fluid dynamics and energy equations and the parameters describing the interactions between the fluid and the solid structures in the porous medium treatment. For this reason, the assembly of the ROM is fast.

### 5.2. Solution of the reduced system

Similarly to the FOM, the ROM equations are solved in a segregated manner, using the nested fixed-point iteration presented in [Fig. 3](#). The flowchart assumes a turbulent flow domain and that every subproblem (fluid dynamics, heat transfer, neutronics) is solved coupled to each other. Furthermore, the iteration strategy showcases a transient problem, while in steady-state scenarios, there is only one step, from the initial guess to the final solution.

The iteration within a time step starts with determining the reduced-order coefficients of the turbulent viscosity and diffusivity which, assuming a two-equation fluid dynamics ROM, is handled by RBF interpolation and depend only on time and model parameters. Therefore, it is enough to compute them once, at the beginning of the iteration. Then, the iteration proceeds with the outer cycle coupling the fluid dynamics, enthalpy and neutronics ROM solvers. To converge the nonlinearities present in the fluid ROM system (i.e., convection term and the flow resistance), an inner cycle has been implemented. In contrast to the FOM, the solution of the fluid dynamics ROM is not segregated, therefore does not need pressure correctors and non-orthogonal correctors. Two additional inner cycles exist to iterate between the fluid dynamics and enthalpy ROMs for cases when the buoyancy effects need to be considered and to resolve the coupling between the energy and neutronics equations.

We see that the adjoint problem, if necessary, is only solved at the end of the time step. The reason behind this is that it requires the converged temperature and velocity fields from the forward problem without affecting any of the equations used to obtain these fields. Every iteration cycle has a corresponding tolerance  $\tau$  which can be set in the input files. The outer iteration terminates when the maximum relative  $l^2$  error in the subproblem-wise reduced coefficients is below  $\tau_{\text{outer}}$ . The initial guesses/conditions for the ROM coefficients of different sub-problems can be obtained by projecting the corresponding initial guesses/conditions of the FOM onto the reduced sub-space. This requires the solution of the following reduced equation:

$$\mathbf{M}_{\Omega}^X \mathbf{c}^X = \mathbf{s}_0, \quad (31)$$

where  $(\mathbf{M}_{\Omega}^X)_{i,j} = \left\langle \psi_i^X, \psi_j^X \right\rangle_{\Omega}$  is a reduced mass matrix, while  $(\mathbf{s}_0)_i = \left\langle \psi_i^X, X_0 \right\rangle_{\Omega}$  with  $X_0$  denoting the FOM initial guess.



**Table 1**

The boundary conditions used for the Full-Order Model (FOM) of the Molten Salt Fast Reactor (MSFR). (Corr. = Corrected).

Field Name	Symbol	Boundary condition
Superficial velocity	$u_D$	$u_D = 0$
Corrected pressure	$p$	$\nabla p \cdot \mathbf{n} = 0$
Scalar flux in energy group $i$	$\phi_i$	$-D_i \nabla \phi_i \cdot \mathbf{n} = \gamma_i \phi_i$
Neutron importance in energy group $i$	$\phi_i^*$	$-D_i \nabla \phi_i^* \cdot \mathbf{n} = \gamma_i \phi_i^*$
Corr. precursor concentration in group $i$	$C_i^*$	$\nabla C_i^* \cdot \mathbf{n} = 0$
Corr. precursor importance in group $i$	$C_i^{*,*}$	$\nabla C_i^{*,*} \cdot \mathbf{n} = 0$
Temperature	$T$	$\nabla T \cdot \mathbf{n} = 0$

**Table 2**

The default values of the thermophysical parameters used for the Molten Salt Fast Reactor.

Parameter name	Symbol	Value
Physical density	$\rho$	4125 $\frac{\text{kg}}{\text{m}^3}$
Molecular viscosity	$\eta$	0.01 Pa s
Specific heat	$c_p$	1600 $\frac{\text{J}}{\text{kg K}}$
Thermal expansion coefficient	$\beta_{th}$	$2 \times 10^{-4} \frac{1}{\text{K}}$
Prandtl number	Pr	8.0

**Table 3**

The default values of the parameters of the porous medium heat exchanger.

Parameter name	Symbol	Value
Fluid fraction	$\gamma$	0.4
Hydraulic diam. of the heat exchanger	$D_h$	0.02 m
Flow res. coefficient in heat exchanger	$A_{f_D}$	0.687
Flow res. exponent in heat exchanger	$B_{f_D}$	-0.25

The heat exchanger is treated as a porous medium zone by homogenizing the structural elements. We assume that the heat exchanger is tubular, thus a Blasius-type correlation (Basse, 2017) can be used to compute the friction factor found in the flow resistance term of Eq. 12, with parameters summarized in Table 3. For the exact expression used to determine the flow resistance term we refer the reader to German et al. (2021). Furthermore, the default steady-state value of the volumetric momentum source used to simulate the pump is  $|F_p| = 80 \frac{\text{KN}}{\text{m}^3}$ .

The reference group constants for the neutronics problems have been generated using Serpent 2 Monte-Carlo particle transport code (Leppänen et al., 2014) from the cross-section libraries available at 900 K with assuming  $\rho_{\text{ref}} = 4125 \frac{\text{kg}}{\text{m}^3}$ . For cases involving temperature feedback phenomena, two additional libraries have been generated: one at 1500 K, with keeping the density at the reference level and another with  $\rho_{\text{pert}} = 3419 \frac{\text{kg}}{\text{m}^3}$  and 900 K. These libraries are utilized to compute the  $\delta$  coefficients in Eq. (21). Altogether six energy groups and eight precursor groups have been used. The energy group structure have been adopted from Fiorina (2013) and German et al. (2019), while the default, 8-group structure of JEFF 3.11 library has been utilized for the precursors.

In case of zero-power problems, we present transient results as well. The transient has been chosen to showcase the effect of a changing velocity field on the neutronics behavior of the system. Since it is part of the FOM, the general structure of the used transient (see Fig. 5) is described here as:

1. The reactor is initially critical with a volumetric pumping force of  $|F_{p,0}| = 30 \frac{\text{KN}}{\text{m}^3}$ . The fields at the initial time step are obtained from a steady-state k-eigenvalue computation.
2. At  $T_0$ , a reactivity insertion occurs which renders the reactor supercritical, but not prompt supercritical. The increase in reactivity is simulated by decreasing  $k_{\text{eff}}$  in the time-dependent multi-group neutron diffusion equations. Note that in the time-dependent scenario  $k_{\text{eff}}$  is just a factor which can modify the fission cross section times the fission neutron yield ( $\nu \Sigma_f$ ) across

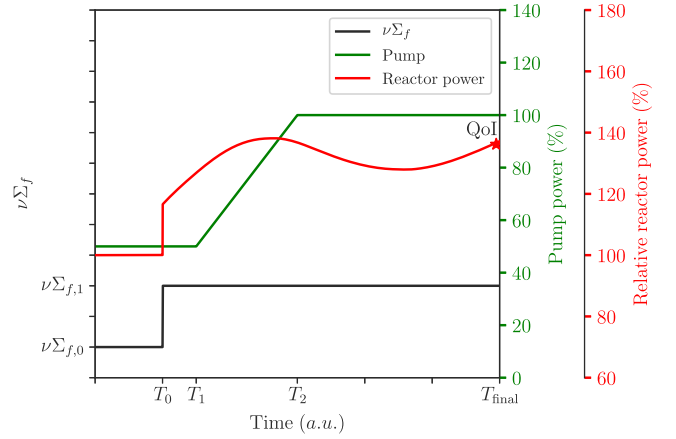


Fig. 5. Timeline of the transients in case of simulations with zero-power MSFR.

the whole reactor. The decrease in this factor leads to an increase in the fission neutron yield.

3. Between  $T_1$  and  $T_2$ , the pumping power is linearly increased to  $|F_p| = F_p$ . This decreases the reactivity by increasing the delayed neutron precursor loss in the high-importance zones of the core.

This transient has been chosen to ascertain whether the ROMs can handle the expected prompt jump in reactor power (due to the reactivity insertion) together with the precursor concentration-driven oscillatory behavior of the power in zero-power conditions.

In case of turbulent flows,  $k - \epsilon$  model is utilized to determine eddy viscosity and diffusivity fields. This requires the solution of two additional equations for the turbulent kinetic energy ( $k$ ) and its dissipation rate ( $\epsilon$ ).

Lastly, the used spatial and temporal discretization schemes are reviewed. The advection term in the momentum equation is discretized using a vanLeer scheme (Van Leer, 1979) which is second order in space. The advection terms in the forward and adjoint precursor equations, enthalpy equations together with those in the  $k - \epsilon$  model are, however, discretized using a first order upwind scheme. The diffusion terms, on the other hand, have been treated using a linear gradient estimator (second order in space) in every equation. The equations are discretized using an implicit Euler scheme in time.

## 6.2. Reduced-order models for zero-power scenarios

First, the applicability of the devised ROM is assessed using zero-power conditions which assume that the temperature-dependence of the neutronics cross sections and the buoyancy effects in the fluid flow do not need to be considered. This means that the examples simplify into a coupled problem between fluid dynamics and neutronics which is optimal for the investigation of the effect of the changing velocity field on the neutronics behavior of the system.

### 6.2.1. Steady-state problem with 13 uncertain model parameters

We start with the investigation of steady-state scenarios. In this case the Quantities of Interest (QoI) are the effective multiplication factor ( $k_{\text{eff}}$ ) and the effective delayed neutron fraction ( $\beta_{\text{eff}}$ ). Since  $\beta_{\text{eff}}$  needs to be computed, the adjoint neutronics problem is to be solved as well. It is assumed that altogether 13 model parameters are uncertain in this case, including the diffusion coefficients, fission cross sections and the pumping power. Therefore the parameter vector can be written as  $\mu = [D_1, \dots, D_6, \nu \Sigma_{f,1}, \dots, \nu \Sigma_{f,6}, |F_p|]$ . The uncertain parameters and their corresponding distributions are summarized in Table 4. In this context,  $\mathcal{U}(a, b)$  denotes the uniform distribution between  $a$  and  $b$ . The upper and lower bounds for the neutronics group constants have been

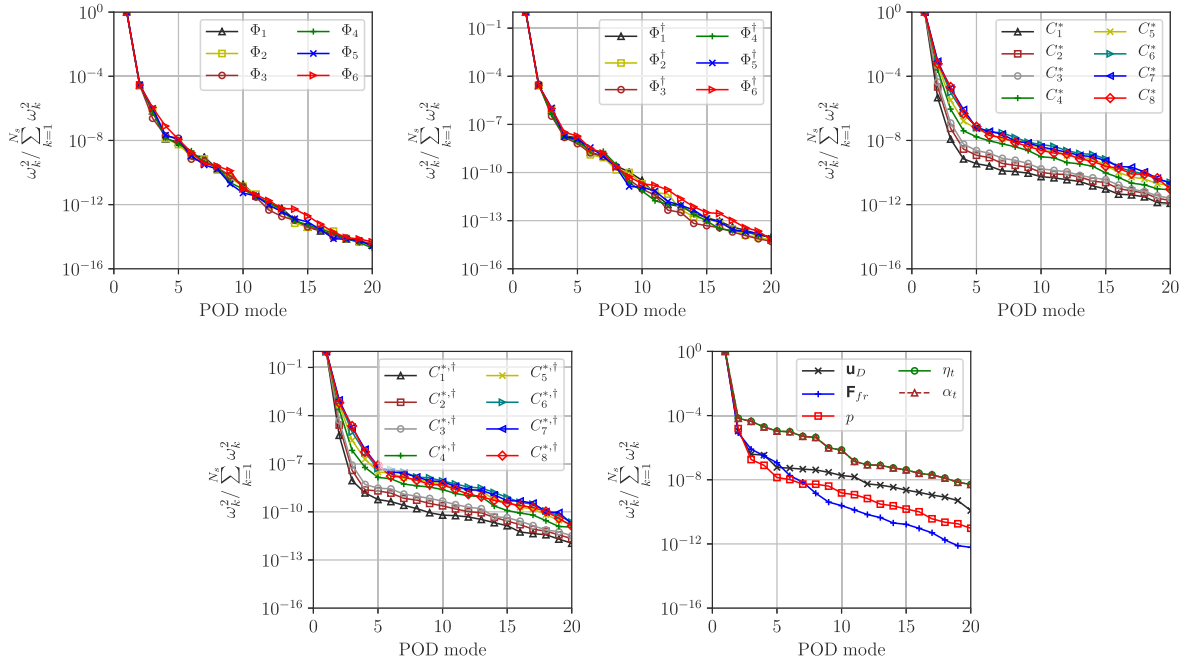


Fig. 6. Scree plots of the normalized squared singular values of the corresponding snapshot matrices obtained from steady-state zero-power simulations.

Table 4

The distributions of the uncertain model parameters for the zero-power steady-state simulations.

Parameter	Distribution	Parameter	Distribution
$D_1$	$\mathcal{U}(0.021, 0.026)$ m	$v\Sigma_{f,1}$	$\mathcal{U}(0.517, 0.633)$ m <sup>-1</sup>
$D_2$	$\mathcal{U}(0.014, 0.017)$ m	$v\Sigma_{f,2}$	$\mathcal{U}(0.338, 0.413)$ m <sup>-1</sup>
$D_3$	$\mathcal{U}(0.009, 0.011)$ m	$v\Sigma_{f,3}$	$\mathcal{U}(0.370, 0.452)$ m <sup>-1</sup>
$D_4$	$\mathcal{U}(0.011, 0.013)$ m	$v\Sigma_{f,4}$	$\mathcal{U}(0.561, 0.685)$ m <sup>-1</sup>
$D_5$	$\mathcal{U}(0.010, 0.012)$ m	$v\Sigma_{f,5}$	$\mathcal{U}(1.320, 1.613)$ m <sup>-1</sup>
$D_6$	$\mathcal{U}(0.010, 0.012)$ m	$v\Sigma_{f,6}$	$\mathcal{U}(4.283, 5.235)$ m <sup>-1</sup>
$ F_p $	$\mathcal{U}(60, 100)$ $\frac{\text{KN}}{\text{m}^2}$		

determined to be the  $\pm 10\%$  values compared to the expected values generated for the reference conditions.

The first step in the generation of the ROMs is the collection of snapshots at different parameter values. Due to the computationally expensive FOM, only 20 instances of  $\mu$  have been drawn using Latin Hypercube Sampling (LHS). After executing the FOM with the prepared model parameter combinations, the steady-state solution fields are saved into corresponding snapshot matrices. Then, spatial global basis functions are extracted by applying POD to the snapshot matrices. The decay in the singular values of the snapshot matrices is a good indicator of the dimensionality of the problem; a fast decay in the singular values suggests that only a few POD modes are sufficient to reconstruct the fields of interest. In many cases, the decay in the squared singular values is more relevant (see Eq. (7)), since it is an indicator of the  $L^2$  error committed by approximating the snapshots by reduced-basis approximates obtained using a simple  $L^2$  projection. Therefore, in this work, the normalized squared singular values are presented in Fig. 6.

It can be observed that the squared singular values of every field decay rapidly, suggesting that the system can be most likely emulated by a low-rank model. This is attributed to the fact that the MSFR is a homogeneous reactor concept with mostly smooth steady-state solution fields. Moreover, we see that the neutron precursor fields with intermediate half-lives (group 1 - longest half-life, group 8 - shortest half-life) require the most basis functions for the reconstruction with a given accuracy. The reason behind this is that precursors with long half-lives, due to their slow nuclear decay, are distributed relatively

evenly in the loop. On the other hand, precursors with very short half-lives, travel very short distances before decaying, thus their distribution does not change considerably with the flow pattern. In the intermediate range, however, the change in the flow significantly modifies the shape of the precursor concentration, which is also expressed by the slower decay of the singular values.

As a next step, multiple ROMs are constructed with different number of extracted basis functions. The accuracy of these ROMs is evaluated using 30 new parameter vectors (test or validation set) drawn using LHS. Based on the observations made in German et al. (2020), namely that the one-equation fluid dynamics ROMs may exhibit stability issues for parametric turbulent flows, a two-equation fluid dynamics ROM has been utilized with supremizer stabilization. Since the supremizer stabilization of the two-equation fluid dynamics ROM may decrease the accuracy in velocity, the utilization of the truncation limit discussed in Section 2 is not optimal for the determination of the number of basis functions. For this reason, an iterative strategy is devised using the test parameter set to optimize the accuracy in velocity using the number of pressure/supremizer modes as input. We note that the number of pressure modes equals to the number of supremizer modes used for every scenario in this work. The iteration strategy starts by increasing the number of velocity and flow resistance modes by one and then the corresponding number of pressure and supremizer modes are determined so that the average relative  $L^2$  error in the velocity is the lowest with maintaining a stable ROM. The number of eddy viscosity and diffusivity modes is determined using a  $\tau = 10^{-6}$  truncation parameter. Below this, the gain in the accuracy of the velocity and precursor concentrations from including additional eddy viscosity and diffusivity modes is negligible. The resulting number of modes and average and maximum  $L^2$  errors over the test set for the final fluid ROM are presented in Table 5. The (+1) means that altogether 1 supremizer mode has been utilized, yielding a total of 3 POD modes for the velocity. The fact that the neutronics subproblems does not influence the fluid dynamics subproblem can justify this segregated approach for the determination of the number of used POD modes.

Using the selected fluid dynamics ROM, a convergence study has been carried out for the neutronics ROM using the validation set and changing the value of the truncation parameter. The corresponding

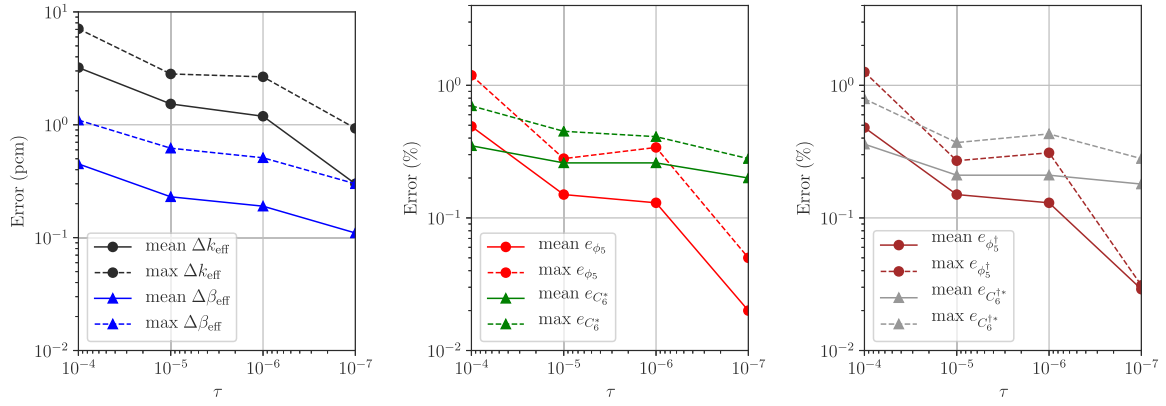


**Fig. 7.** Error statistics over the validation set as function of the truncation limit for the quantities of interest (left), representative fields of the forward (middle) and adjoint (right) neutronics problem.

**Table 5**

The number of POD modes used for the fluid ROM together with the average and maximum errors over the test set in case of zero-power steady-state simulations.

Field	Rank	$\bar{e}$ (%)	max( $e$ ) (%)
$u_D$	2 (+1)	0.34	0.68
$p$	1	0.42	0.92
$v_i$	10	0.13	0.50
$\alpha_i$	10	0.13	0.50

**Table 6**

The number of basis functions used for the construction of the neutronics ROM with  $\tau = 10^{-7}$  for zero-power steady-state simulations.

Field	Rank	Field	Rank	Field	Rank	Field	Rank
$\phi_1$	3	$C_2^*$	2	$\phi_7^*$	3	$C_2^{*+}$	2
$\phi_2$	3	$C_3^*$	3	$\phi_8^*$	3	$C_3^{*+}$	3
$\phi_3$	3	$C_4^*$	3	$\phi_9^*$	3	$C_4^{*+}$	4
$\phi_4$	3	$C_5^*$	5	$\phi_{10}^*$	3	$C_5^{*+}$	5
$\phi_5$	3	$C_6^*$	6	$\phi_{11}^*$	3	$C_6^{*+}$	6
$\phi_6$	3	$C_7^*$	5	$\phi_{12}^*$	3	$C_7^{*+}$	5
$C_1^*$	2	$C_8^*$	5	$C_1^{*+}$	2	$C_8^{*+}$	5

errors over the validation set are shown in Fig. 7. It is visible that overall the mean error decreases with the decreasing truncation limit.

The final model which corresponds to  $\tau = 10^{-7}$  yields an average error in the effective multiplication factor and effective delayed neutron fraction of 0.3 pcm and 0.11 pcm with the maximum errors being 0.93 pcm and 0.3 pcm, respectively. Furthermore, the  $L^2$  error of every field of interest is below 0.28%. The number of modes used for the neutronics ROM built using  $\tau = 10^{-7}$  is presented in Table 6. It can be observed that 2–6 modes are enough to reconstruct the solution fields with an acceptable accuracy.

We note that solving a steady-state fluid problem together with forward and adjoint neutronics eigenvalue problems took 4400 s on average, while the execution time of the ROM is 0.19 s. This means that the ROM yields speed-up factors around  $2.3 \times 10^5$ . Lastly, we investigate how the number of captured snapshots influences the accuracy of the generated ROMs. For this, an experiment has been carried out where the number of employed snapshots is either 10, 20 or 30. The ROMs in this experiment are generated by using the same number of velocity, pressure and supremizer modes as presented in Table 5 with the number of  $\eta_i$  and  $\alpha_i$  modes determined using  $\tau = 10^{-6}$ . The number of modes for the neutronics fields has been determined using  $\tau = 10^{-7}$ . The error statistics from the experiment over the same 30-sample test set are shown in Table 7.

It can be observed, with the exception of the pressure (heavily influenced by the supremizer field), that the errors slightly decrease with the increasing snapshots used for the training. However, we note

that the ROM built using 10 snapshots only already yields excellent results, meaning that the original training cost could have been further reduced.

### 6.2.2. Transient problem with 2 uncertain model parameters

The next example showcases ROMs for the transient scenario introduced in Fig. 5. In this scenario, we define two uncertain model parameters: the step change in the effective multiplication factor ( $\delta k_{\text{eff}}$ ) at the beginning of the transient and the relative pumping force ( $a_{F_p} = \frac{F_p}{|F_{F,0}|}$ ) at the end of the ramp. The corresponding distributions are presented in Table 8.

Furthermore, the step change in  $k_{\text{eff}}$  is applied at  $T_0 = 0$  s, while we start the ramp in the pumping force at  $T_1 = 1$  s and end it at  $T_2 = 4$  s. The transient simulations are terminated at  $T_{\text{final}} = 6$  s. The transient is solved using an adaptive time-stepping based on the change in reactor power to ensure proper resolution at regions where the solution fields change rapidly. The quantity of interest, as indicated in Fig. 5, is the relative reactor power (normalized by the initial power) at the end of the simulation. The generation of the ROMs for the transient scenario introduced in Fig. 5 starts with the collection of snapshots. For this, 9 transients are carried out with different model parameter vectors drawn using a LHS design. Fig. 8 showcases the relative power curves of the training transients. Throughout these transients, fields of interest have been captured every 0.03 s, yielding altogether 1,800 snapshots per field. The spatial global basis functions have been synthesized from the snapshots using the POD process discussed in Section 2. Again, two-equation fluid ROMs are utilized for the simulations. The decay in the squared singular values of the snapshot matrices is shown in Fig. 9.

We see a steep decay in the singular values of the group fluxes indicating that the shape of the neutron flux does not change significantly over time. This entails that only a few basis functions will be enough to approximate these fields. Moreover, we see that the precursor concentrations and fluid dynamics fields exhibit a considerably slower decay suggesting that many basis functions are needed for an accurate approximation.

Following this, multiple ROMs have been prepared with different numbers of basis functions. These ROMs are then tested using 10 additional test parameter vectors which do not overlap with the ones used for the training of the ROMs. Due to the accuracy concerns of the supremizer stabilization, the number of basis functions in the fluid dynamics ROM has not been determined using the truncation limit in Section 2. Instead, an iterative strategy has been implemented which aims at finding the best average accuracy in velocity over the test set. In the iterative process, the number of eddy viscosity modes has been fixed to 37 which corresponds to  $\tau = 10^{-5}$ . The number of basis functions selected by the iterative method for the fluid dynamics fields is presented in Table 9 together with the corresponding average

**Table 7**  
Error statistics of representative fields over the 30-sample test set for ROMs built using 10/20/30 snapshots.

$N_s$	$e_{u_D}$ (%)	$e_p$ (%)	$e_{v_i}$ (%)	$e_{\alpha_i}$ (%)	$e_{\phi_s}$ (%)	$e_{C_c}$ (%)	$\Delta k_{\text{eff}}$ (pcm)
10	0.34/0.94	0.42/0.87	1.03/5.88	1.03/5.88	0.02/0.05	0.22/0.35	0.31/0.93
20	0.34/0.68	0.42/0.92	0.13/0.50	0.13/0.50	0.02/0.05	0.20/0.28	0.30/0.93
30	0.34/0.59	0.42/0.94	0.08/0.11	0.08/0.11	0.02/0.04	0.20/0.28	0.30/0.92

**Table 8**  
The distributions of the 23 uncertain model parameters for the zero-power transient simulations.

Parameter	Symbol	Distribution
Change in $k_{\text{eff}}$	$\delta k_{\text{eff}}$	$\mathcal{U}(25,55)$ pcm
Relative increase in pumping force	$a_{F_p}$	$\mathcal{U}(2.0,3.33)$

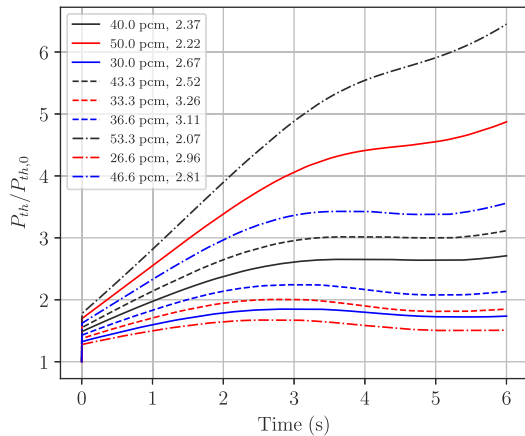


**Fig. 8.** Relative reactor power as function of time for the training transients in case of zero-power simulations.

**Table 9**  
The number of used POD modes for the fluid dynamics ROM together with the resulting average and maximum errors over the test set in case of transient zero-power simulations.

Field	Rank	$\bar{e}$ (%)	$\max(e)$ (%)
$u_D$	16 (+3)	1.84	4.22
$p$	3	1.55	9.53
$v_i$	37	5.60	31.84
$\alpha_i$	37	5.60	31.84

and maximum  $L^2$  errors over the transients in the test set. Again, the (+3) for  $u_D$  indicates that 3 supremizer modes have been used for the stabilization of the ROM. Even though the corresponding errors are not analyzed here, we note that altogether 6 basis functions have been used for the discrete empirical interpolation of the flow resistance. Similarly to the steady-state scenario, we can justify the standalone optimization of the fluid dynamics ROM with the fact that the neutronics subproblem does not influence the fluid dynamics fields due to the zero-power approximation.

It can be observed that the RBF interpolation for the eddy viscosity/diffusivity gives high errors which propagate to the other fields of interest as well. This is the result of the advection dominated problem not being smooth in time and parameter space together with the fact that  $9 \times 200$  interpolation points are not sufficient for the resolution of the problem. However, adding more interpolation points considerably increases the number of evaluations and therefore the runtime of the ROM. This issue is further discussed in Section 6.4.

Once the fluid dynamics ROM has been finalized, the number of basis functions used for the neutronics ROM can be determined using the energy retention parameter (see Eq. (7)). Fig. 10 presents the maximum and average relative errors in the QoI and several representative

**Table 10**  
The number of basis functions used for the construction of the neutronics ROM with  $\tau = 10^{-3}$  for zero-power transient simulations.

Field	Rank	Field	Rank
$\phi_1$	1	$C_2^*$	2
$\phi_2$	1	$C_3^*$	3
$\phi_3$	1	$C_4^*$	3
$\phi_4$	1	$C_5^*$	3
$\phi_5$	1	$C_6^*$	3
$\phi_6$	1	$C_7^*$	2
$C_1^*$	1	$C_8^*$	2

neutronics fields over the test set (over all times and parameter values) for ROMs built with different values of  $\tau$ . We see that the best ROM in terms of the QoI is the one built using  $\tau = 10^{-3}$ . Furthermore, it can be observed that the average errors in the representative field decrease with the increasing number of basis functions, however this increase in accuracy is negligible beyond  $\tau = 10^{-3}$ . The reason behind this can be the propagation of the error in eddy diffusivity/viscosity directly through the precursor equations and indirectly through the inaccuracy in velocity. The sources of these errors are further discussed in Section 6.4. Nevertheless, at  $\tau = 10^{-3}$ , the average and maximum relative errors in the QoI are slightly more than 1% and 3%, respectively. Table 10 presents the number of basis functions used for the neutronics subproblem for  $\tau = 10^{-3}$ .

Lastly, the computational speedup is assessed. Since an adaptive time-stepping scheme has been used, the runtimes for the FOMs varied considerably depending on the relative change in reactor power. Using one core of a processor, the FOM required 4,600–26,000 s per transient. The execution time of the ROM changed in the 59–120 s interval, which results in an approximate speed-up factor of 78–216. The reason behind this moderate (compared to the steady-state case) gain is the RBF interpolation of 37 turbulent viscosity and diffusivity modes at  $9 \times 200$  anchor points at every time step. Possible improvements could be the utilization of the sparsity in the interpolation or utilizing the fact that the time scale of the change in turbulent viscosity is much longer compared to that of the neutronics fields at sudden jumps such as the initial event in the selected transient.

### 6.3. Reduced-order model for nominal-power scenarios

As a third example, we present ROMs for steady-state fully-coupled simulations for nominal-power scenarios. This means that both the buoyancy effects in the fluid flow and the temperature-dependence of the neutron group constants are considered. To increase the complexity of the problem, additional uncertain model parameters have been added to the 13 parameters of the zero-power scenario. The uncertain model parameters and their corresponding distributions are listed in Table 11. The quantity of our interest in this case, is the effective multiplication factor of the system ( $k_{\text{eff}}$ ). We see that  $\Sigma_r$  removal cross sections are considered to be uncertain. This cross section can be expressed in terms of other reaction cross sections as:  $\Sigma_{r,g} = \Sigma_{t,g} - \Sigma_{s,g \rightarrow g}$ . Furthermore, only the reference values of the cross sections are assumed to be uncertain, the  $\delta_{FD}$ ,  $\delta_{FT}$  coefficients describing their temperature-dependence are fixed values.

As before, the generation of ROMs begins with the collection of snapshots of different fields of interest. In this example, we save snapshots of the velocity ( $u_D$ ), the corrected pressure ( $p$ ), the eddy viscosity

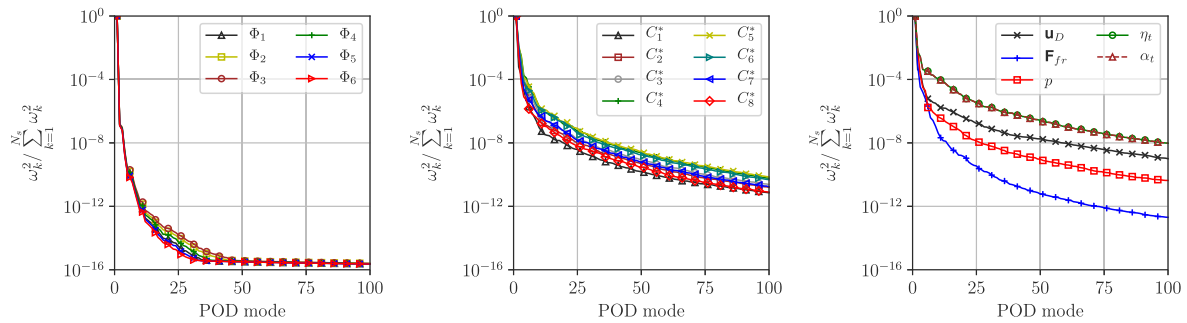


Fig. 9. Scree plots of the normalized squared singular values of the corresponding snapshot matrices obtained from transient zero-power simulations.

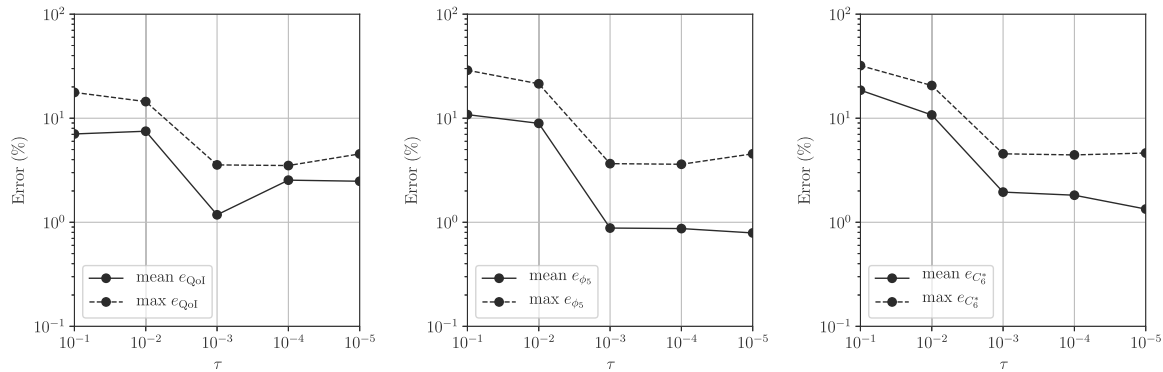


Fig. 10. Error statistics over the validation set as function of the truncation limit for the quantities of interest (left), scalar flux in group 5 (middle) and precursor concentration in group 6 (right).

**Table 11**  
The distributions of the uncertain model parameters for the nominal-power steady-state simulations.

Parameter	Distribution	Parameter	Distribution
$D_1$	$\mathcal{U}(0.021, 0.026)$ m	$\nu \Sigma_{f,1}$	$\mathcal{U}(0.517, 0.633)$ m <sup>-1</sup>
$D_2$	$\mathcal{U}(0.014, 0.017)$ m	$\nu \Sigma_{f,2}$	$\mathcal{U}(0.338, 0.413)$ m <sup>-1</sup>
$D_3$	$\mathcal{U}(0.009, 0.011)$ m	$\nu \Sigma_{f,3}$	$\mathcal{U}(0.370, 0.452)$ m <sup>-1</sup>
$D_4$	$\mathcal{U}(0.011, 0.013)$ m	$\nu \Sigma_{f,4}$	$\mathcal{U}(0.561, 0.685)$ m <sup>-1</sup>
$D_5$	$\mathcal{U}(0.010, 0.012)$ m	$\nu \Sigma_{f,5}$	$\mathcal{U}(1.320, 1.61)$ m <sup>-1</sup>
$D_6$	$\mathcal{U}(0.010, 0.012)$ m	$\nu \Sigma_{f,6}$	$\mathcal{U}(4.283, 5.235)$ m <sup>-1</sup>
$\Sigma_{r,1}$	$\mathcal{U}(6.210, 7.590)$ $\frac{1}{\text{cm}}$	$ F_p $	$\mathcal{U}(60, 100)$ $\frac{\text{KN}}{\text{m}^2}$
$\Sigma_{r,2}$	$\mathcal{U}(3.560, 4.351)$ $\frac{1}{\text{m}}$	$T_{\text{hx}}$	$\mathcal{U}(850, 950)$ K
$\Sigma_{r,3}$	$\mathcal{U}(1.597, 1.952)$ $\frac{1}{\text{m}}$	$\alpha_{\text{hx}}$	$\mathcal{U}(0.8 \times 10^5, 1.2 \times 10^5)$ $\frac{\text{W}}{\text{m}^2 \text{K}}$
$\Sigma_{r,4}$	$\mathcal{U}(1.785, 2.182)$ $\frac{1}{\text{cm}}$	$\beta_{\text{th}}$	$\mathcal{U}(1.8 \times 10^{-4}, 2.2 \times 10^{-4})$ $\frac{1}{\text{K}}$
$\Sigma_{r,5}$	$\mathcal{U}(1.474, 1.801)$ $\frac{1}{\text{cm}}$	Pr	$\mathcal{U}(7.2, 8.8)$
$\Sigma_{r,6}$	$\mathcal{U}(3.210, 3.923)$ $\frac{1}{\text{cm}}$		

( $\nu_i$ ) and diffusivity ( $\alpha_i$ ), the flow-resistance in the heat exchanger ( $F_{\text{fr}}$ ) together with the scalar flux in each energy group ( $\phi_i$ ,  $i = 1, \dots, 6$ ), the corrected precursor concentrations ( $C_i^*$ ,  $i = 1, \dots, 8$ ), the temperature ( $T$ ) and the logarithmic temperature ( $\log(T)$ ). Due to the fact that the FOM is computationally expensive to solve and we observed in the zero-power scenario that the problem is relatively smooth in parameter space, we assume that capturing 30 snapshots is enough. The following test results will support this assumption. The 30 training parameter vectors have been drawn using LHS. The global spatial basis functions for the fields of interest are then extracted from these snapshots using POD. The decay in the squared singular values of the different fields of interest is presented in Fig. 11.

We see that the singular values decay fast meaning that the solutions can be approximated using only a few basis functions. Therefore, multiple ROMs have been prepared with different values of the truncation parameter ( $\tau$ ) to test the behavior of the proposed method. The number of basis functions in the fluid dynamics ROM have been determined

by first selecting the number of velocity modes using the truncation parameter and then optimizing the number of pressure and supremizer modes to get the best accuracy in velocity. Additionally, due to the large parameter space and the low sensitivity of the eddy viscosity and diffusivity to the parameters in the neutronics and enthalpy equations, the RBF interpolation has been restricted to the pumping power alone. For testing purposes 20 new parameter vectors have been drawn using LHS. The FOM and the different ROMs are executed using these parameters and the results are compared. The truncation parameter-dependent error statistics over the test set are presented in Fig. 12.

It can be observed that the ROM built using  $\tau = 10^{-10}$  is capable of emulating the QoI with an average and maximum error of 10 pcm and 14 pcm, respectively. We see that there is a considerable increase in error between  $\tau = 10^{-4}$  and  $\tau = 10^{-6}$ , which can be explained by the inclusion of additional spatial basis functions for the temperature while not including more basis functions for the auxiliary temperature. Once the number of POD modes is increased for the auxiliary temperature field, the error starts to decrease. The increasing average error (the maximum error is still decreasing) is attributed to the errors introduced by the fluid dynamics ROMs, which is further discussed in Section 6.4. To prove this, an experiment is carried out where the number of basis functions are kept for the fluid dynamics fields at the  $\tau = 10^{-7}$  level, while retaining modes with  $\tau = 10^{-8}$  and  $\tau = 10^{-10}$  for every additional field. The results of this experiment are presented in Table 12. We see that the ROM built with  $\tau = 10^{-10}$  for every additional field yields errors lower than 1.35% in every scenario. Furthermore, this ROM yields average and maximum absolute errors in  $k_{\text{eff}}$  of 3.14 pcm and 9.10 pcm, respectively. This is considered to be a significant improvement over the 10.37, 14.14 pcm values obtained using the higher-dimensional fluid ROM (last points in Fig. 12). The number of modes used with the low-dimensional fluid ROM coupled with the highest dimensional energy and neutronics ROMs is presented in Table 13. We see that 2–18 modes are sufficient to describe the system with adequate accuracy.

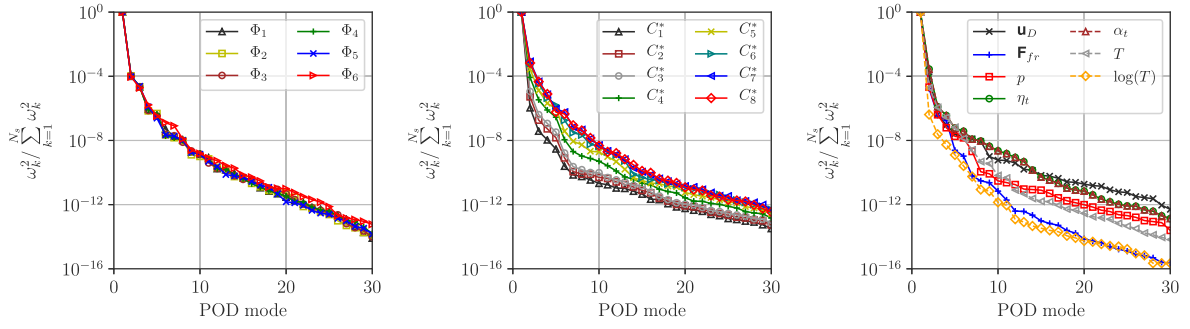


Fig. 11. Scree plots of the normalized squared singular values of the corresponding snapshot matrices obtained from steady-state nominal-power simulations.

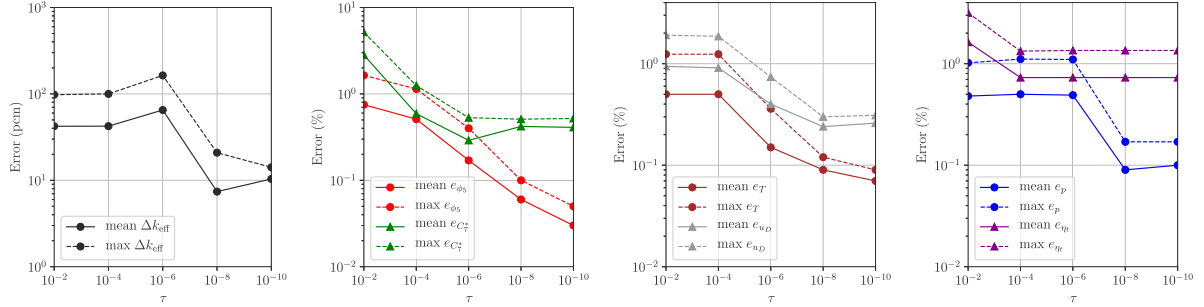


Fig. 12. Error statistics over the validation set as function of the truncation limit for the quantities of interest and representative fields of interest.

Table 12

The field statistics of the representative fields over the validation test set in case of steady-state nominal-power simulations using the lower-dimensional ( $\tau = 10^{-7}$ ) fluid ROM.

$\tau$	$\overline{e_{\phi_5}}$ (%)	$\max(e_{\phi_5})$ (%)	$\overline{e_{C_7}}$ (%)	$\max(e_{C_7})$ (%)	$\overline{e_T}$ (%)	$\max(e_T)$ (%)
$10^{-8}$	0.03	0.05	0.31	0.38	0.09	0.14
$10^{-10}$	0.02	0.04	0.31	0.38	0.08	0.13

$\tau$	$\overline{e_{u_D}}$ (%)	$\max(e_{u_D})$ (%)	$\overline{e_p}$ (%)	$\max(e_p)$ (%)	$\overline{e_{v_i}}$ (%)	$\max(e_{v_i})$ (%)
$10^{-8}$	0.15	0.21	0.10	0.16	0.73	1.35
$10^{-10}$	0.15	0.21	0.10	0.16	0.73	1.35

Table 13

The number of basis functions used for the construction of the final ROMs for the nominal-power steady-state simulations. The ranks correspond to  $\tau = 10^{-7}$  for the fluid dynamics fields and  $\tau = 10^{-10}$  for every additional field.

Field	Rank	Field	Rank	Field	Rank	Field	Rank
$\phi_1$	15	$C_1^*$	9	$C_7^*$	18	$\alpha_t$	8
$\phi_2$	15	$C_2^*$	11	$C_8^*$	17	$T$	10
$\phi_3$	14	$C_3^*$	12	$u_D$	4 (+2)	$\log(T)$	6
$\phi_4$	15	$C_4^*$	14	$p$	2		
$\phi_5$	15	$C_5^*$	16	$F_{fr}$	4		
$\phi_6$	16	$C_6^*$	17	$v_i$	8		

Since only global error indicator have been presented so far, Figs. 13–16 show the local errors in the representative fields at the first parameter point in the test set using the ROM with the best accuracy. We see that the maximum error in the velocity is approximately 3 orders of magnitude lower compared to the characteristic velocity ( $1-2 \frac{m}{s}$ ) of the original solution.

Similarly, maximum error in temperature is 2.73 K with the maximum temperature being 1268 K. We see an even better match in terms of the scalar flux in group 5; the maximum errors are approximately 4 orders of magnitude lower than the maximum flux value.

We see that the highest error is located close to the symmetry axis of the model. This can be explained by the inaccuracy in the temperature in this region. The precursor concentration in group 7, however, show higher errors which are only 2 orders of magnitude

lower than the maximum concentrations. To put the achieved results into perspective, we compare the performance of the intrusive POD-RB ROMs to the non-intrusive, POD-based, sparse-grid interpolation-based ROMs in Alsayyari et al. (2020). The ROMs presented in Alsayyari et al. (2020) for the MSFR showed a maximum  $l^2$  error of 0.02% in temperature and 37 pcm in  $k_{eff}$ . The same are 0.13% and 9.1 pcm for the intrusive ROM in this work. It must be mentioned, however, that while the non-intrusive ROM required 63 and 1639 model evaluations for the temperature and  $k_{eff}$ , the intrusive ROM needs only 30. We note, however, that the two examples are not one-to-one comparable due to the differences in the used FOMs and the chosen model parameters.

Lastly, the computational speedup is assessed for using the selected ROM instead of the corresponding FOM. Due to the slow convergence and the fact that a pseudo-transient is used to obtain the steady-state results with the FOM, it takes 21,000 s on average for a single execution. The solution time of the ROM, however, takes only 1.25 s on average, yielding an approximate speedup factor of 16,800.

#### 6.4. Some notes on ROM accuracy

As experienced throughout the numerical examples, some of the developed ROMs have a limited accuracy which can be the result of the following factors:

1. The supremizer stabilization of the fluid dynamics ROM may decrease the accuracy of the velocity. Since the supremizer velocity modes do not have a physical meaning, their overuse may decrease the accuracy in the velocity field. This can be an issue for problems that require a large number of basis functions for the accurate reconstruction of the pressure, as this would require the addition of an equal number of supremizer modes to the velocity subspace. A solution to this inconvenience can be the development of a numerically consistent, reduced-order equivalent of the PIMPLE algorithm (Star et al., 2020). In certain scenarios, using the one-equation fluid dynamics ROM implemented in GeN-ROM (initially published in Lorenzi et al. (2016)) might yield more accurate results, but it often exhibits stability issues for turbulent simulations.

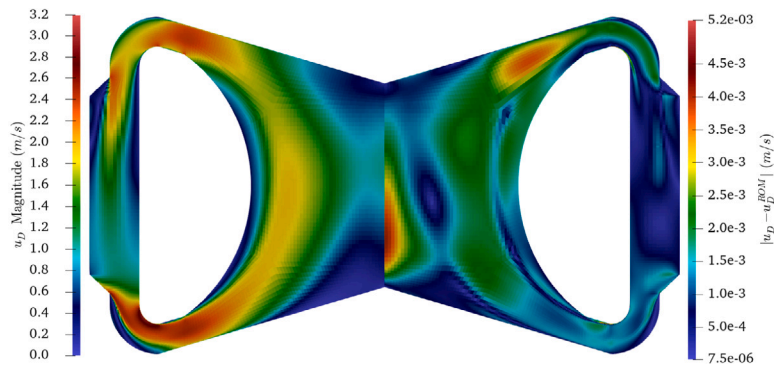


Fig. 13. The velocity field of the FOM (left) together with the absolute error between the FOM and the ROM (right) for the first sample in the validation set used for the fully-coupled simulations of the MSFR.

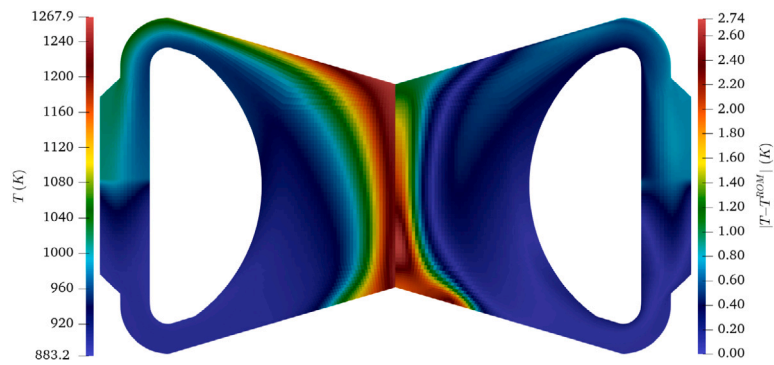


Fig. 14. The temperature fields of the FOM (left) together with the absolute error between the FOM and the ROM (right) for the first sample in the validation set used for the fully-coupled simulations of the MSFR.

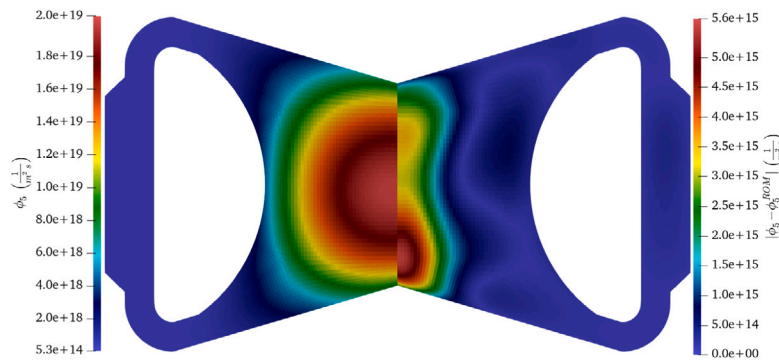


Fig. 15. The representative scalar flux of the FOM (left) together with the absolute error between the FOM and the ROM (right) for the first sample in the validation set used for the fully-coupled simulations of the MSFR.

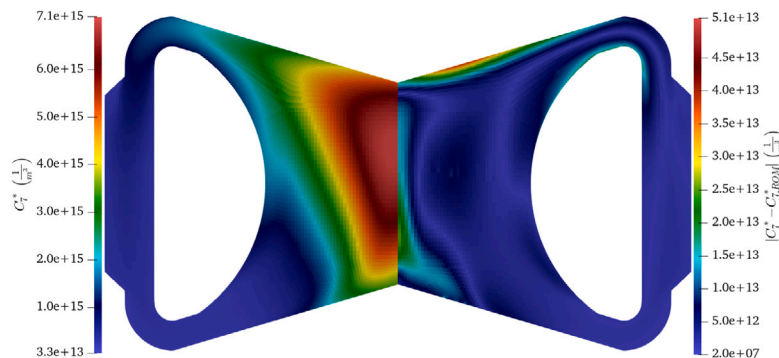


Fig. 16. The representative precursor concentration of the FOM (left) together with the absolute error between the FOM and the ROM (right) for the first sample in the validation set used for the fully-coupled simulations of the MSFR.

2. The RBF interpolation of the eddy viscosity and diffusivity fields can cause considerable errors, especially when the number of training data points is limited or the number of model parameters is high. This error then propagates to the other solution fields through the diffusion terms. As showcased in the transient problem, the interpolation in time may require a lot of anchor nodes to yield reasonable accuracy. However, the cost of the evaluation of the RBF interpolant scales with the number of anchor points, considerably slowing down the reduced-order model. Therefore, we conclude that the RBF-based approach is better suited for steady-state problems.
3. The use of first-order upwind schemes for the discretization of the advection terms in the scalar transport equations may decrease the accuracy of the ROM. The reason behind this is that the discretization of the advection terms depends on the actual solution for the velocity:  $\nabla \cdot (u_D X)$ . However, the elements of the reduced advection operators (see Eq. (26) for example) are computed using the  $\psi_i^{u_D}$ , which describe different flow patterns compared to the original solution. This introduces a numerical inconsistency which may lead to errors for advection-dominated problems on coarse meshes. This error can be negligible for problems with fine meshes, diffusion dominated systems (laminar flows), or higher-order upwind schemes.
4. The use of Galerkin projection for discretized time-dependent nonlinear systems is not optimal. This may be a contributor to the relatively high errors experienced for the time-dependent example in this work. For more information about the mathematical basis of this error and a possible solution using Petrov–Galerkin projection, see Carlberg et al. (2017).

## 7. Summary and conclusions

In this paper, we have introduced an intrusive Model Order Reduction (MOR) technique for parametric multiphysics problems in liquid-fuel Molten Salt Reactors (MSRs). The developed method aims at reducing the computational costs associated with multi-query applications (e.g., uncertainty quantification or design optimization) which are essential parts of the design and licensing of nuclear systems. The method is based on the Proper Orthogonal Decomposition aided Reduced-Basis (POD-RB) technique combined with the method of snapshots. This entails that global spatial basis functions are generated for the fields of interest by applying POD to a set of snapshots captured while exercising the Full-Order Model (FOM). These basis functions are then used to reduce the dimensionality of the problem by a Galerkin projection of the governing equations. To ensure the computational efficiency of the ROMs, the affine decomposition of the operators in the FOM and the Discrete Empirical Interpolation method (DEIM) have been extensively utilized. In this work, the porous medium Reynolds-Averaged Navier Stokes (RANS) equations are reduced together with the porous medium enthalpy equation. These are coupled with the multigroup neutron diffusion equations and precursor transport equations from the neutronics side. To the best of the authors' knowledge, the following contributions are novel in this work:

1. The development of a POD-RB-ROM for coupled neutronics and thermal hydraulics simulations in a porous medium setting. This allows the modeling of homogenized structural elements in the nuclear systems.
2. The implementation of the method in an OpenFOAM®-based framework, GeN-ROM, for both steady-state and transient problems, with turbulent and laminar flow regimes for realistic Molten Salt Reactor geometries.
3. The addition of the reduced adjoint neutronics equations and their utilization to compute important reactor parameters such as the effective delayed neutron fraction.

4. The extension of German et al. (2019) for modeling reactivity density feedback.

The developed method has been tested using a 2D axisymmetric model of the Molten Salt Fast Reactor. Multiple steady-state and a transient scenarios have been investigated. We see that the best steady-state ROMs yield accurate results with the maximum  $L^2$  error being below 1.35% across all fields of interest and cases studied. This error is acceptable when compared to the geometry, physics, and operating condition errors incurred throughout the generation of numerical models for liquid-fuel reactors. The errors for transient problems, however, are significantly higher and can attain 31% for auxiliary fields like the eddy viscosity. The maximum errors for the most important solution fields, however still remain below 9.54% with the maximum mean error being 5.60%. The achieved single-run speedups are on the order of  $10^4 - 10^5$  for steady-state computations, while a moderate 78–216 has been obtained for transient problems. Based on these, we conclude, that the developed ROMs, in turbulent flow regimes are better suited for steady-state simulations. The potential reasons behind this are discussed in Section 6.4 in detail.

Future work may include the development and implementation of new approaches to improve eddy viscosity and diffusivity models at the reduced-order level, together with more robust stabilized ROMs for the fluid dynamics subproblem.

## Declaration of competing interest

The authors declare that they have no known competing financial interests or personal relationships that could have appeared to influence the work reported in this paper.

## Acknowledgments

This material is based upon work supported under an NEUP-IRP Award of the Department of Energy, Office of Nuclear Energy (contract reference DE-NE0008651).

## Appendix A. Derivation of the reduced fluid dynamics equations

This section serves as an example of how to derive reduced-order equations. For demonstration purposes, the following expression shows the scalar product notation of this process using a Laplacian term in an arbitrary governing equation:

$$\langle \psi_i^X, \Delta \psi_j^X \rangle_{\Omega} = \sum_{k=1}^N \psi_{i,k}^X L_k \psi_j^X V_k = \psi_i^{X,T} \mathbf{M}_{\Omega} (L \psi_j^X), \quad (\text{A.1})$$

where  $\langle \cdot, \cdot \rangle_{\Omega}$  denotes a volumetric integral. This is equivalent to the matrix–matrix product notation used in Section 2. In a finite volume setting, the inner product can be transformed into a  $\mathbf{M}_{\Omega}$  weighted matrix–matrix product, also highlighted in Eq. (A.1). The fluid dynamics equations are selected for this purpose. The process starts with the approximations of the fields of interest. First, we approximate the velocity and pressure fields as:

$$u_D \approx \tilde{u}_D = \sum_{i=1}^{r_{u_D}} \psi_i^{u_D} c_i^{u_D} = \Psi^{u_D} c^{u_D}, \quad \text{and} \quad p \approx \tilde{p} = \sum_{i=1}^{r_p} \psi_i^p c_i^p = \Psi^p c^p. \quad (\text{A.2})$$

Note, for ease of notation, the function representation of the fields is used. However, the following derivation has an equivalent linear algebra-based derivation as well. For the connection between the two, see Eq. (A.1). Following this, with the assumption that the fluid flow is in turbulent regime, we approximate the eddy viscosity and diffusivity as:

$$\eta_t \approx \tilde{\eta}_t = \sum_{i=1}^{r_{\eta_t}} \psi_i^{\eta_t} c_i^{\eta_t} = \Psi^{\eta_t} c^{\eta_t}, \quad \text{and} \quad \alpha_t \approx \tilde{\alpha}_t = \sum_{i=1}^{r_{\alpha_t}} \psi_i^{\alpha_t} c_i^{\alpha_t} = \Psi^{\alpha_t} c^{\alpha_t}. \quad (\text{A.3})$$

If the problem involves porous medium zones with non-negligible flow resistances, we approximate the volumetric obstructing force in zone  $z$  as:

$$\mathbf{F}_{f,r,z} \approx \tilde{\mathbf{F}}_{f,r,z} = \sum_{i=1}^{r_{f,r,z}} \psi_i^{F_{f,r,z}} c_i^{F_{f,r,z}} = \Psi^{F_{f,r,z}} \mathbf{c}^{F_{f,r,z}}. \quad (\text{A.4})$$

Lastly, the temperature is approximated as:

$$T \approx \tilde{T} = \sum_{i=1}^{r_T} \psi_i^T c_i^T = \Psi^T \mathbf{c}^T. \quad (\text{A.5})$$

As a next step, we take these approximations and plug them back into the governing equations described by Eqs. 11–12. Then, the momentum equation is projected using the velocity basis functions, while the continuity equation is projected using the pressure basis functions to arrive at the following form:

$$\left\langle \psi_i^{u_D}, \frac{\partial \rho \tilde{u}_D}{\partial t} + \frac{1}{\gamma} \nabla \cdot (\rho \tilde{u}_D \otimes \tilde{u}_D) - \nabla \cdot \left( (\eta + \tilde{\eta}) \left[ \nabla \tilde{u}_D + (\nabla \tilde{u}_D)^T \right] \right) + \gamma \nabla \tilde{p} - \gamma \mathbf{F}_p - \gamma \tilde{\mathbf{F}}_{f,r} - \gamma \beta_{th} \rho \mathbf{g} \cdot \mathbf{r} \nabla \tilde{T} \right\rangle_{\Omega} = 0 \quad i = 1, \dots, r_{u_D}, \quad (\text{A.6})$$

$$\langle \psi_i^p, \nabla \cdot \rho \tilde{u}_D \rangle_{\Omega} = 0, \quad i = 1, \dots, r_p. \quad (\text{A.7})$$

Once this form is at hand, one can expand the reduced-basis approximates and carry out the integrals for every basis function pair to obtain the expressions for the reduced operators and source terms in Eqs. (24)–(25). For the one-equation fluid dynamics ROM implemented in GeN-ROM, only the momentum equation is reduced with the assumption of:  $c_i^{u_D} = c_i^p = c_i^{\eta}$ . In this scenario, however, the basis functions of  $p$  and  $\eta$  are obtained slightly differently. For more information on the differences and similarities between the one- and two-equation ROMs, see German et al. (2020) and German (2021).

## Appendix B. Handling of the boundary conditions

For the handling of the boundary conditions, we use the diffusion term in Eq. (14), which can be expressed using the cell-centered finite volume approach in OpenFOAM® (Jasak, 1996) as:

$$[\nabla \cdot (D_g \nabla \phi_g)]_P \approx \frac{\sum_f D_{g,f} \nabla \phi_{g,f} \cdot \mathbf{S}_f}{V_P}, \quad (\text{B.1})$$

where  $P$  denotes the cell-center values,  $f$  the face values and  $\mathbf{S}$  the surface normal area vector. If the cell happens to be on the boundary of the domain, this expression turns into:

$$\frac{\sum_f D_{g,f} \nabla \phi_{g,f} \cdot \mathbf{S}_f}{V_P} = \frac{\sum_f^{N_i} D_{g,f} \nabla \phi_{g,f} \cdot \mathbf{S}_f}{V_P} + \frac{\sum_f^{N_b} C_{\text{int}}^{\text{BC}} \phi_{g,f} \mathbf{S}_f}{V_P} + \frac{\sum_f^{N_b} C_{\text{ext}}^{\text{BC}} \mathbf{S}_f}{V_P}, \quad (\text{B.2})$$

where  $N_i$  and  $N_b$  denote the internal and boundary faces of the cell. Coefficients  $C_{\text{int}}^{\text{BC}}$  and  $C_{\text{ext}}^{\text{BC}}$  are boundary condition-dependent and add terms on the diagonal and to the source term of the linear system. For homogeneous Robin boundary conditions (albedo)  $C_{\text{ext}}^{\text{BC}} = 0$  and  $C_{\text{int}}^{\text{BC}} = \gamma_r$ , for homogeneous Neumann conditions (reflective) both  $C_{\text{int}}^{\text{BC}} = C_{\text{ext}}^{\text{BC}} = 0$ , while for homogeneous Dirichlet conditions  $C_{\text{ext}}^{\text{BC}} = 0$  and  $C_{\text{int}}^{\text{BC}} = \frac{1}{\Delta_f}$ , where  $\Delta_f$  denotes the distance between the centers of the cell and the boundary face. Given that this treatment is applied to every cell in the mesh, the reduced diffusion term in Eq. (27) can be expressed as:

$$\left( \sum_{z=1}^{N_z} -D_g^z \mathbf{K}_g^z \right) \mathbf{c}^{\phi_g} + \left( \sum_{b=1}^{N_{\text{BC}}} \mathbf{K}_g^{\text{int},b} \right) \mathbf{c}^{\phi_g} + \left( \sum_{b=1}^{N_{\text{BC}}} \mathbf{k}_g^{\text{ext},b} \right), \quad (\text{B.3})$$

where the elements of the modified reduced terms are computed using the reduced-basis approximates together with a Galerkin projection. In the expression above,  $(\mathbf{K}_g^{\text{int},b})$  is a contribution to the reduced system

matrix, while  $(\mathbf{k}_g^{\text{ext},b})$  contributes to the reduced source term. This practice has been followed for every differential operator whenever necessary in the presented examples. Even though it is not used in this work, we note that GeN-ROM uses a penalty treatment to enforce non-homogeneous Dirichlet boundary conditions for the velocity field in the momentum equation. For more information about this approach, we refer the reader to Lorenzi et al. (2016) and German et al. (2020).

## Appendix C. Efficient computation of $\beta_{\text{eff}}$ at the ROM level

For problems, where the quantity of interest is the effective delayed neutron fraction ( $\beta_{\text{eff}}$ ), an efficient way to evaluate Eq. (19) has been developed. The following expression gives the group-wise contributions to  $\beta_{\text{eff}}$  directly using the expansion coefficients of the forward flux ( $\mathbf{c}^{\phi_g}$ ), precursor concentrations ( $\mathbf{c}^{C_i^*}$ ) and adjoint flux ( $\mathbf{c}^{\phi_g^{\dagger}}$ ) together with operators of reduced size:

$$\beta_{\text{eff},i} = \frac{\sum_{g=1}^{G_e} \mathbf{c}^{\phi_g^{\dagger},T} \left( \sum_{z=1}^{N_z} \chi_{d,g}^z \lambda_i^z \mathbf{A}_{g,i}^z \right) \mathbf{c}^{C_i^*}}{\sum_{g=1}^{G_e} \mathbf{c}^{\phi_g^{\dagger},T} \left[ \sum_{j=0}^{N_z} \left( \sum_{z=1}^{N_z} \chi_{d,g}^z \lambda_j^z \mathbf{A}_{g,j}^z \right) \mathbf{c}^{C_j^*} + \sum_{g'=1}^{G_e} \left( \sum_{z=1}^{N_z} \chi_{p,g}^z \nu_{g'}^z \Sigma_{f,g'}^z \mathbf{F}_{g,g'}^z \right) \mathbf{c}^{\phi_{g'}^{\dagger}} \right]}, \quad (\text{C.1})$$

where the entries of the reduced operators can be computed as:

$$\left( \mathbf{A}_{g,i}^z \right)_{i,j} = \left\langle \psi_i^{\phi_g^{\dagger}}, \delta_z(\mathbf{r}) \gamma \psi_j^{C_i^*} \right\rangle_{\Omega} \quad \text{and} \\ \left( \mathbf{F}_{g,g'}^z \right)_{i,j} = \left\langle \psi_i^{\phi_g^{\dagger}}, \delta_z(\mathbf{r}) \psi_j^{\phi_{g'}^{\dagger}} \right\rangle_{\Omega}. \quad (\text{C.2})$$

## Appendix D. DEIM-based treatment of temperature-dependent cross sections

Taking a general reaction term  $\Sigma \phi_g$  together with the expression of the temperature-dependent group constant in Eq. (21), we can derive the following expansion:

$$\left( \sum_{z=1}^{N_z} \Sigma_{\text{ref}}^z \mathbf{M}_{g,g}^z + \delta_{FT}^z \left( \mathbf{c}^{T_{\text{aux}},T} \overline{\mathbf{A}}_{FT,g}^z - T_{\text{ref}}^{\text{aux}} \mathbf{M}_{g,g}^z \right) + \delta_{FD}^z \beta_{th} \rho \left( \mathbf{c}^{T,T} \overline{\mathbf{A}}_{FD,g}^z - T_{\text{ref}} \mathbf{M}_{g,g}^z \right) \right) \mathbf{c}^{\phi_g}, \quad (\text{D.1})$$

where  $\mathbf{M}_{g,g}^z$  is defined at Eq. (27) and the rest of the reduced operators can be computed using the following expressions:

$$\left( \overline{\mathbf{A}}_{FD,g}^z \right)_{i,j,k} = \left\langle \psi_i^{\phi_g^{\dagger}}, \delta_z(\mathbf{r}) \psi_k^T \psi_j^{\phi_g} \right\rangle_{\Omega}, \\ \left( \overline{\mathbf{A}}_{FT,g}^z \right)_{i,j,k} = \left\langle \psi_i^{\phi_g^{\dagger}}, \delta_z(\mathbf{r}) \psi_k^{T_{\text{aux}}} \psi_j^{\phi_g} \right\rangle_{\Omega}. \quad (\text{D.2})$$

## References

- Abdi, H., 2007. Singular value decomposition (SVD) and generalized singular value decomposition. In: Encyclopedia of Measurement and Statistics. pp. 907–912.
- Alsayyari, F., Tibergh, M., Perkó, Z., Lathouwers, D., Kloosterman, J.L., 2020. A nonintrusive adaptive reduced order modeling approach for a molten salt reactor system. Ann. Nucl. Energy 141, 107321.
- Aufiero, M., Brovchenko, M., Cammi, A., Clifford, I., Geoffroy, O., Heuer, D., Laureau, A., Losa, M., Luzzi, L., Merle-Lucotte, E., et al., 2014. Calculating the effective delayed neutron fraction in the molten salt fast reactor: analytical, deterministic and Monte Carlo approaches. Ann. Nucl. Energy 65, 78–90.
- Ballarin, F., Manzoni, A., Quarteroni, A., Rozza, G., 2015. Supremizer stabilization of POD–Galerkin approximation of parametrized steady incompressible Navier–Stokes equations. Internat. J. Numer. Methods Engrg. 102 (5), 1136–1161.
- Basse, N.T., 2017. Turbulence intensity and the friction factor for smooth-and rough-wall pipe flow. Fluids 2 (2), 30.
- Behne, P., Ragusa, J., Morel, J., 2016. Model order reduction for sn radiation transport. In: Proceedings of M&C2019, Portland, OR, USA. pp. 2481–2491.
- Buchan, A.G., Calloo, A., Goffin, M.G., Dargaville, S., Fang, F., Pain, C.C., Navon, I.M., 2015. A POD reduced order model for resolving angular direction in neutron/photon transport problems. J. Comput. Phys. 296, 138–157.

- Buchan, A., Pain, C., Fang, F., Navon, I., 2013. A POD reduced-order model for eigenvalue problems with application to reactor physics. *Internat. J. Numer. Methods Engrg.* 95 (12), 1011–1032.
- Carlberg, K., Barone, M., Antil, H., 2017. Galerkin v. least-squares Petrov–Galerkin projection in nonlinear model reduction. *J. Comput. Phys.* 330, 693–734.
- Chaturantab, S., Sorensen, D.C., 2010. Nonlinear model reduction via discrete empirical interpolation. *SIAM J. Sci. Comput.* 32 (5), 2737–2764.
- Duderstadt, J.J., Hamilton, L.J., 1976. *Nuclear Reactor Analysis*. 1976. John Wiley & Sons, NY.
- Fiorina, C., 2013. *The Molten Salt Fast Reactor as a Fast-Spectrum Candidate for Thorium Implementation* (Ph.D. thesis). Politecnico di Milano, [https://www.politesi.polimi.it/bitstream/10589/74324/1/2013\\_03\\_PhD\\_Fiorina.pdf](https://www.politesi.polimi.it/bitstream/10589/74324/1/2013_03_PhD_Fiorina.pdf).
- Fiorina, C., Aufiero, M., Cammi, A., Guerrieri, C., Krepel, J., Luzzi, L., Mikityuk, K., Ricotti, M.E., 2012. Analysis of the MSFR core neutronics adopting different neutron transport models. In: *International Conference on Nuclear Engineering*, Vol. 44991. American Society of Mechanical Engineers, pp. 219–228.
- Fiorina, C., Clifford, I., Aufiero, M., Mikityuk, K., 2015. GeN-Foam: a novel OpenFOAM® based multi-physics solver for 2D/3D transient analysis of nuclear reactors. *Nucl. Eng. Des.* 294, 24–37.
- Fiorina, C., Kerkar, N., Mikityuk, K., Rubiolo, P., Pautz, A., 2016. Development and verification of the neutron diffusion solver for the GeN-Foam multi-physics platform. *Ann. Nucl. Energy* 96, 212–222.
- Fiorina, C., Lathouwers, D., Aufiero, M., Cammi, A., Guerrieri, C., Kloosterman, J.L., Luzzi, L., Ricotti, M.E., 2014. Modelling and analysis of the MSFR transient behaviour. *Ann. Nucl. Energy* 64, 485–498.
- Georgaka, S., Stabile, G., Star, K., Rozza, G., Bluck, M.J., 2020. A hybrid reduced order method for modelling turbulent heat transfer problems. *Comput. & Fluids* 208, 104615.
- German, P., 2021. *Multiphysics Model Order Reduction for Molten Salt Reactors*, PhD dissertation, Texas A & M University (Ph.D. thesis). Texas A&M University.
- German, P., Ragusa, J.C., 2019. Reduced-order modeling of parameterized multi-group diffusion k-eigenvalue problems. *Ann. Nucl. Energy* 134, 144–157.
- German, P., Ragusa, J.C., Fiorina, C., 2019. Application of multiphysics model order reduction to doppler/neutronic feedback. *EPJ Nucl. Sci. Technol.* 5, 17.
- German, P., Tano, M.E., Fiorina, C., Ragusa, J.C., 2021. Data-driven reduced-order modeling of convective heat transfer in porous media. *Fluids* 6 (8), <http://dx.doi.org/10.3390/fluids6080266>, URL <https://www.mdpi.com/2311-5521/6/8/266>.
- German, P., Tano, M., Ragusa, J.C., Fiorina, C., 2020. Comparison of Reduced-Basis techniques for the model order reduction of parametric incompressible fluid flows. *Prog. Nucl. Energy* 130, 103551.
- Gerner, A.-L., Veroy, K., 2012. Certified reduced basis methods for parametrized saddle point problems. *SIAM J. Sci. Comput.* 34 (5), A2812–A2836.
- Hesthaven, J.S., Rozza, G., Stamm, B., et al., 2016. *Certified Reduced Basis Methods for Parametrized Partial Differential Equations*. Springer.
- Hijazi, S., Ali, S., Stabile, G., Ballarin, F., Rozza, G., 2018. The effort of increasing Reynolds number in projection-based reduced order methods: from laminar to turbulent flows. *arXiv preprint arXiv:1807.11370*.
- Hijazi, S., Stabile, G., Mola, A., Rozza, G., 2019. Data-driven POD-Galerkin reduced order model for turbulent flows. *arXiv preprint arXiv:1907.09909*.
- Jasak, H., 1996. *Error Analysis and Estimation for the Finite Volume Method with Applications to Fluid Flows*. ICL (Ph.D. thesis, Ph.D. thesis). Imperial College London (University of London).
- Jasak, H., Jemcov, A., Tukovic, Z., et al., 2007. OpenFOAM: A C++ library for complex physics simulations. In: *International Workshop on Coupled Methods in Numerical Dynamics*, Vol. 1000. IUC Dubrovnik Croatia, pp. 1–20.
- Leppänen, J., Pusa, M., Viitanen, T., Valtavirta, V., Kalliaiseno, T., 2014. The Serpent Monte Carlo code: Status, development and applications in 2013. In: *SNA+ MC 2013-Joint International Conference on Supercomputing in Nuclear Applications+ Monte Carlo*. EDP Sciences, pp. 6–21.
- Lorenzi, S., 2018. An adjoint proper orthogonal decomposition method for a neutronics reduced order model. *Ann. Nucl. Energy* 114, 245–258.
- Lorenzi, S., Cammi, A., Luzzi, L., Rozza, G., 2016. POD-Galerkin method for finite volume approximation of Navier–Stokes and RANS equations. *Comput. Methods Appl. Mech. Engrg.* 311, 151–179.
- Lorenzi, S., Cammi, A., Luzzi, L., Rozza, G., 2017. A reduced order model for investigating the dynamics of the Gen-IV LFR coolant pool. *Appl. Math. Model.* 46, 263–284.
- Panico, D.M., 2019. *Development of C++ tool for Reduced Order Modelling of the Molten Salt Fast Reactor multiphysics: Sensitivity Analysis Application* (MSc Thesis).
- Pearson, K., 1901. LIII. On lines and planes of closest fit to systems of points in space. *Lond. Edinb. Dublin Philos. Mag. J. Sci.* 2 (11), 559–572.
- Pinnau, R., 2008. *Model reduction via proper orthogonal decomposition*. In: *Model Order Reduction: Theory, Research Aspects and Applications*. Springer, pp. 95–109.
- Prince, Z.M., Ragusa, J.C., 2019. Parametric uncertainty quantification using proper generalized decomposition applied to neutron diffusion. *Internat. J. Numer. Methods Engrg.* 119 (9), 899–921.
- Radman, S., Fiorina, C., Pautz, A., 2021. Development of a novel two-phase flow solver for nuclear reactor analysis: algorithms, verification and implementation in OpenFOAM. *Nucl. Eng. Des.* 379, 111178.
- Ragusa, J.C., Mahadevan, V.S., 2009. Consistent and accurate schemes for coupled neutronics thermal-hydraulics reactor analysis. *Nucl. Eng. Des.* 239 (3), 566–579.
- Ribes, A., Caremoli, C., 2007. Salome platform component model for numerical simulation. In: *31st Annual International Computer Software and Applications Conference (COMPSAC 2007)*, Vol. 2. IEEE, pp. 553–564.
- Rouch, H., Geoffroy, O., Rubiolo, P., Laureau, A., Brovchenko, M., Heuer, D., Merle-Lucotte, E., 2014. Preliminary thermal–hydraulic core design of the Molten Salt Fast Reactor (MSFR). *Ann. Nucl. Energy* 64, 449–456.
- Santanoceto, M., Tibergh, M., Perkó, Z., Dulla, S., Lathouwers, D., 2021. Preliminary uncertainty and sensitivity analysis of the Molten Salt Fast Reactor steady-state using a polynomial chaos expansion method. *Ann. Nucl. Energy* 159, 108311.
- Sartori, A., Baroli, D., Cammi, A., Luzzi, L., Rozza, G., 2014. A reduced order model for multi-group time-dependent parameterized reactor spatial kinetics. In: *2014 22nd International Conference on Nuclear Engineering*. American Society of Mechanical Engineers, V005T17A048.
- Sartori, A., Cammi, A., Luzzi, L., Rozza, G., 2016. A multi-physics reduced order model for the analysis of lead fast reactor single channel. *Ann. Nucl. Energy* 87, 198–208.
- Shi, J., Fratoni, M., 2021. Gen-foam model and benchmark of delayed neutron precursor drift in the molten salt reactor experiment. In: *EPJ Web of Conferences*, Vol. 247. EDP Sciences, p. 06040.
- Sirovich, L., 1987. Turbulence and the dynamics of coherent structures. III. Dynamics and scaling. *Quart. Appl. Math.* 45, 583–590.
- Stabile, G., Hijazi, S., Mola, A., Lorenzi, S., Rozza, G., 2017. POD-Galerkin reduced order methods for CFD using Finite Volume Discretisation: vortex shedding around a circular cylinder. *arXiv preprint arXiv:1701.03424*.
- Stabile, G., Rozza, G., 2018. Finite volume POD-Galerkin stabilised reduced order methods for the parametrised incompressible Navier–Stokes equations. *Comput. & Fluids* 173, 273–284.
- Star, S.K., Sanderse, B., Stabile, G., Rozza, G., Degroote, J., 2020. Reduced order models for the incompressible Navier–Stokes equations on collocated grids using a ‘discretize-then-project’ approach. *arXiv preprint arXiv:2010.06964*.
- Star, K., Stabile, G., Georgaka, S., Belloni, F., Rozza, G., Degroote, J., 2019. POD-Galerkin reduced order model of the Boussinesq approximation for buoyancy-driven enclosed flows. In: *M&C 2019. American Nuclear Society (ANS)*, pp. 2452–2461.
- Sun, Y., Yang, J., Wang, Y., Li, Z., Ma, Y., 2020. A POD reduced-order model for resolving the neutron transport problems of nuclear reactor. *Ann. Nucl. Energy* 149, 107799.
- Tano, M., German, P., Ragusa, J., 2021a. Evaluation of pressure reconstruction techniques for model order reduction in incompressible convective heat transfer. *Therm. Sci. Eng. Prog.* 23, 100841.
- Tano, M., Ragusa, J., Caron, D., Behne, P., 2021b. Affine reduced-order model for radiation transport problems in cylindrical coordinates. *Ann. Nucl. Energy* 158, 108214.
- Tano Retamales, M., 2018. *Développement des Modèles Multi-Physiques Multi-échelle de Caloporteurs sels Fondus à Haute Température et Validation Expérimentale* (Ph.D. thesis). Grenoble Alpes.
- Van Leer, B., 1979. Towards the ultimate conservative difference scheme. V. A second-order sequel to Godunov’s method. *J. Comput. Phys.* 32 (1), 101–136.
- Vergari, L., Cammi, A., Lorenzi, S., 2020. Reduced order modeling approach for parametrized thermal-hydraulics problems: inclusion of the energy equation in the POD-FV-ROM method. *Prog. Nucl. Energy* 118, 103071.
- Vergari, L., Cammi, A., Lorenzi, S., 2021. Reduced order modeling for coupled thermal-hydraulics and reactor physics problems. *Prog. Nucl. Energy* 140, 103899.
- Wang, M., Wang, Y., Tian, W., Qiu, S., Su, G., 2021. Recent progress of CFD applications in PWR thermal hydraulics study and future directions. *Ann. Nucl. Energy* 150, 107836.